Structural basis of interdomain communication in PPARγ

Sarah A. Mosure [1,2,#], Paola Munoz-Tello [1,#], Kuang-Ting Kuo [2,3], Brian MacTavish [1], Xiaoyu Yu [1,2], Daniel Scholl [4], Christopher C. Williams [1,2], Timothy S. Strutzenberg [2,3], Jared Bass [1], Richard Brust [1], Ashok A. Deniz [4], Patrick R. Griffin [1,3], & Douglas J. Kojetin [1,3,*]

[1] Department of Integrative Structural and Computational Biology, UF Scripps Biomedical Research, Jupiter, Florida 33458, USA
[2] Skaggs Graduate School of Chemical and Biological Sciences at Scripps Research, Jupiter, FL 33458, USA
[3] Department of Molecular Medicine, UF Scripps Biomedical Research, Jupiter, Florida 33458, USA
[4] Department of Integrative Structural and Computational Biology, The Scripps Research Institute, La Jolla, California 92037, USA
[#] These authors contributed equally.
* Corresponding author: dkojetin@ufl.edu

ABSTRACT

PPARγ is a nuclear receptor transcription factor that regulates adipogenic and insulin sensitizing gene programs via two activation function (AF) regulatory domains: a ligand-dependent AF-2 coregulator interaction surface within the C-terminal ligand-binding domain (LBD) and an N-terminal disordered AF-1 domain (NTD or A/B region). Here, we show the AF-1 contains an evolutionary conserved Trp-Pro motif that populates two long-lived AF-1 conformations via proline *cis/trans* isomerization. The Trp-Pro motif participates in transient intradomain AF-1 contacts and interdomain contacts with two surfaces of the LBD (β-sheet and AF-2). Mutagenesis indicates the Pro residue negatively regulates PPARγ transcriptional output, suggesting a potential regulatory mechanism for AF-1 isomerization. Our findings provide a structural rationale to explain previous *in vitro* and cellular studies that reported interdomain functional communication between the PPARγ AF-1 and LBD. Our study also illuminates a structural biology platform to study how disordered domains in nuclear receptors influence their structure and function.

INTRODUCTION

Peroxisome proliferator-activated receptor gamma (PPARγ; NR1C3) is a nuclear receptor transcription factor that controls gene expression programs influencing the differentiation of mesenchymal stem cells into adipocytes (adipogenesis), lipid metabolism, and insulin sensitivity. Like other nuclear receptors [1], PPARγ is a multidomain protein that contains a central DNA-binding domain flanked by two regulatory regions that influence transcription: an N-terminal ligand-independent AF-1 domain (also called the NTD or A/B region) and a C-terminal ligand-dependent AF-2 coregulator interaction surface within the C-terminal LBD.

The molecular and structural basis of ligand-regulated functions of the LBD of nuclear receptors are relatively well understood. For PPARγ, structural biology studies including X-ray crystallography, hydrogen-deuterium mass spectrometry (HDX-MS), chemical crosslinking MS (XL-MS), and NMR spectroscopy have revealed how agonist ligands stabilize a transcriptionally active AF-2/helix 12 surface conformation upon binding to the orthosteric ligand-binding pocket in the LBD to promote coactivator protein recruitment and increased expression of PPARγ target genes that drive adipogenesis [2–6]. More recently, we reported a structural mechanism of ligand-dependent corepressor-selective PPARγ inverse agonism [7]. We defined the transcriptionally repressive AF-2/helix 12 conformation that promotes corepressor interaction and transcriptional repression of PPARγ. We also identified the apo-LBD conformation that dynamically exchanges between active- and repressive-like conformations [8].

Despite these and other key advances in determining ligand-dependent structural mechanisms of nuclear receptor LBD function, the structural basis by which the disordered N-terminal AF-1 influences the function of PPARγ and other nuclear receptors remains poorly understood. Only a few crystal structures of full-length nuclear receptors including PPARγ have been reported and these structures either lack electron density for the disordered AF-1 or the AF-1 was removed to facilitate crystallization [9–12]. Cryo-EM studies of nuclear receptors thus far have only provided low resolution (>10–25Å) structural snapshots of the AF-1 or, similar to the crystallography studies, protein samples were used where the AF-1 was removed [13–16]. Furthermore, AlphaFold [17] models of nuclear receptors frequently show cloud-like AF-1/NTD structural depictions that are thought to be an artifact of the computational method to avoid steric clashes with structured domains [18].

Obtaining atomic resolution structural data on the PPARγ AF-1 would be important for the field—new regulatory mechanisms are likely to emerge, and the data may explain published observations of interdomain functional communication between the PPARγ AF-1 and AF-2/LBD. For example, PPARγ transcription and PPARγ-mediated adipogenesis is increased by AF-1 removal, indicating the AF-1 negatively regulates PPARγ transcription [19]. Phosphorylation of Ser112 within the AF-1 negatively affects LBD functions (ligand binding and coregulator interaction), downregulates the expression of PPARγ target genes, and inhibits adipogenesis [20–23]. Furthermore, phosphorylation of Ser112 in the AF-1 is inhibited by an agonist ligand binding to the LBD that stabilizes a transcriptionally active AF-2 surface conformation, but not by an inverse agonist that stabilizes a transcriptionally repressive LBD conformation [24]. These observations suggest that the N-terminal AF-1 somehow alters the structure and function of the C-terminal LBD, and vice versa, though currently there is no structural evidence into the molecular mechanism.

To gain molecular insight into how the disordered AF-1 regulates PPARγ function, we used biophysical and structural biology approaches suitable for studying intrinsically disordered proteins (IDPs) including ^{1}H- and ^{13}C-detected NMR spectroscopy, single-molecule FRET (smFRET), and XL-MS. Our studies uncovered several previously unknown structural features of the AF-1 that are poised to regulate the structure and function of PPARγ. We uncovered a region of the AF-1 that natively exchanges between two long-lived structural conformations resulting from proline *cis/trans* isomerization at a Trp-Pro motif. Although the AF-1 is structurally disordered, our studies reveal intradomain contacts within the AF-1 indicating it adopts a partially compact conformational ensemble. Finally, we show that the LBD physically interacts with the AF-1, including the region containing the slowly exchanging Trp-Pro motif. Our findings provide a structural mechanism to explain previous reports of interdomain functional communication.

RESULTS

AF-1 is a structurally disordered domain

Bioinformatic sequence analysis of full-length human PPARγ2 isoform (**Figure 1A**), whose expression is mostly restricted to adipocytes [25], predicts the AF-1 domain (A/B region; residues 1-135) is structurally disordered (**Figure 1B**). Experimental support for the disordered nature of the AF-1 comes from high solvent exchange observed by HDX-MS

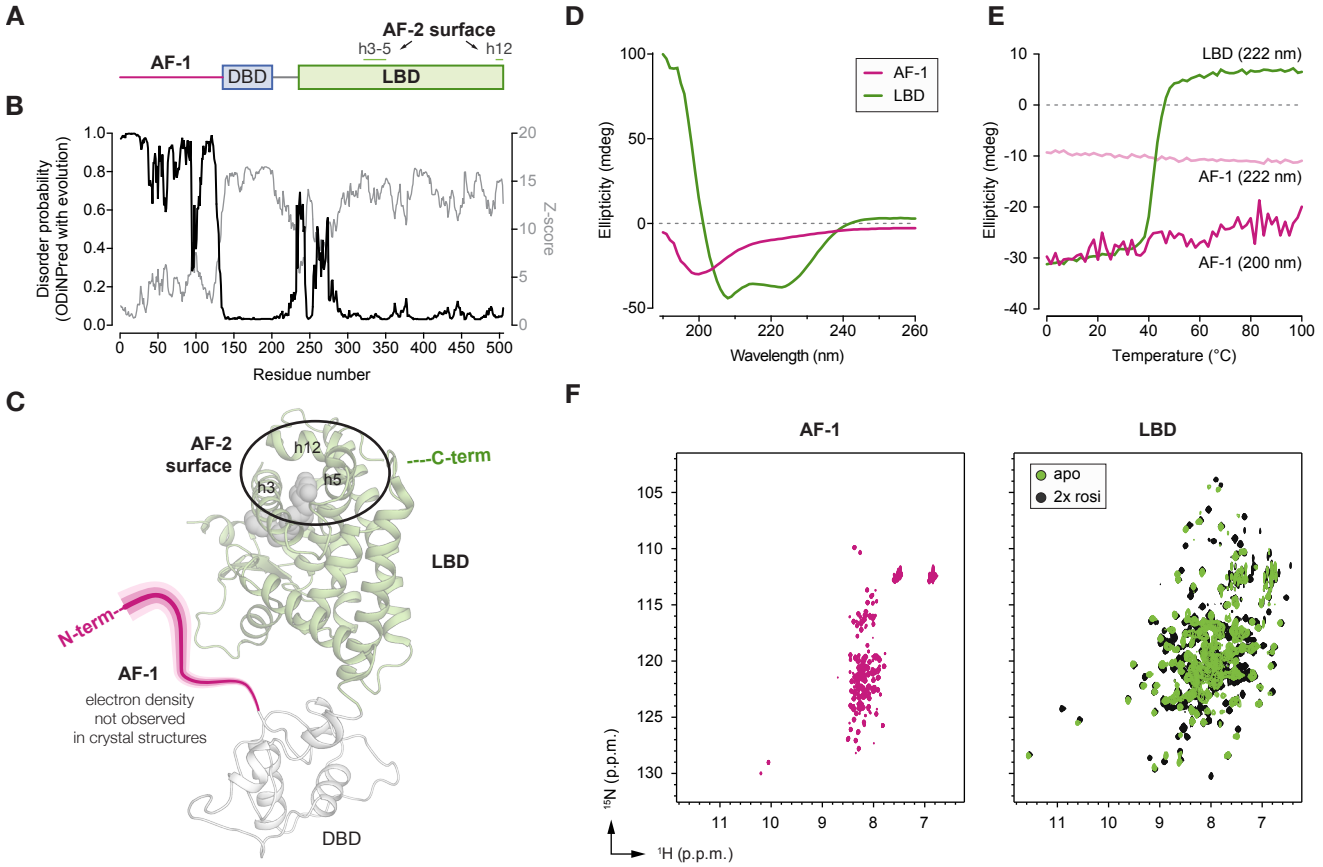

Figure 1. Biophysical comparison of the PPARγ AF-1 and LBD structural properties.
(**A**) Domain architecture of human PPARγ isoform 2 (PPARγ2).
(**B**) Disorder prediction plot of PPARγ2.
(**C**) Crystal structure of full-length PPARγ (PDB 3DZY, chain D) highlighting the LBD (green) and the msising disordered AF-1 (pink).
(**D**) Circular dichroism (CD) spectra of AF-1 and LBD.
(**E**) Temperature-dependent CD thermal denaturation data of AF-1 and LBD.
(**F**) 2D [^{1}H,^{15}N]-HSQC NMR spectrum of AF-1 (left) and 2D [^{1}H,^{15}N]-TROSY-HSQC NMR spectra of LBD in the apo and rosiglitazone-bound forms (right).

[11], which likely explains why crystal structures that include full-length PPARγ do not show AF-1 electron density [11] (**Figure 1C**). To provide further experimental support, we compared the isolated AF-1 and LBD using circular dichroism (CD) spectroscopy methods, which report on secondary structure features present in proteins [26] and temperature-dependent protein foldedness [27]. CD spectral analysis (**Figure 1D**) of the AF-1 shows a random coil profile characteristic of a disordered protein, whereas the LBD shows a profile consistent with its three-layer α-helical sandwich fold [1]. CD collected as a function of temperature (**Figure 1E**) shows a well-defined unfolding transition for the LBD, whereas the AF-1 shows no notable cooperative unfolding transition.

Comparison of 2D [^{1}H,^{15}N]-HSQC NMR spectra of the AF-1 and LBD (**Figure 1F**) reveals the AF-1 displays poor amide spectral dispersion characteristic of a disordered protein, whereas the LBD—a structured three-layer α-helical sandwich fold that is stabilized upon ligand binding [6, 28]—shows well dispersed amide chemical shifts. ^{15}N{^{1}H} heteronuclear NOE analysis reveals low values for the AF-1 (**Figure S1A**) compared to the LBD (**Figure S1B**), indicating the AF-1 possesses higher amplitude motions on the ps-ns timescale, which is characteristic of IDPs. Analysis of backbone Cα and Cβ NMR chemical shifts, which can predict secondary structure in IDPs and folded proteins [29], reveals AF-1 regions with low α-helical and β-sheet propensity (**Figure S1C**) compared to the robust secondary structure present in the LBD (**Figure S1D**). CD analysis of the AF-1 in the presence of increasing trifluoroethanol (TFE) shows an increase in α-helical signature (**Figure S1E**). Taken together, these data indicate that although the AF-1 is structurally disordered, there are regions with transient or lowly populated secondary structure.

Charge repulsion influences AF-1 compactness

Disordered proteins can either adopt extended conformations with no intradomain contacts or compact conformational ensembles with transient or robust intradomain contacts— structural features that can be detected using paramagnetic relaxation enhancement (PRE) NMR methods [30]. Using site directed mutagenesis, we introduced a cysteine residue at several locations in the AF-1, which lacks native cysteine residues, and attached the cysteine-reactive nitroxide spin label MTSL to each construct (D11C, S22C, D33C, D61C, A91C, S112C). We collected 2D [^{1}H,^{15}N]-HSQC NMR data in the paramagnetic and diamagnetic state and calculated peak intensity ratios ($I_{PRE} = I_{para}/I_{dia}$) to reveal AF-1 residues that are in close structural proximity to the MTSL label (**Figure 2A**). Generally, residues with $I_{PRE} = 0$ correspond to a distance <12Å, and $I_{PRE} > 0$ and < 1 correspond to a distance between 13-25Å where the peak intensity decrease is proportional to $1/r^6$ from the unpaired electron [31]. I_{PRE} values of the MTSL spin label at D11 near the N-terminus (D11C-MTSL) are consistent with an extended conformation with no significant long-range contacts as the profile is similar to a predicted I_{PRE} profile from an extended AF-1 ensemble calculated using *flexible-meccano* [32]. In contrast, MTSL placement at other regions within the AF-1 reveals long-range contacts given the experimental I_{PRE} values deviate from predicted extended I_{PRE} AF-1 profiles. The experimental PRE NMR profiles indicate the most robust intradomain interactions occur for residues where the

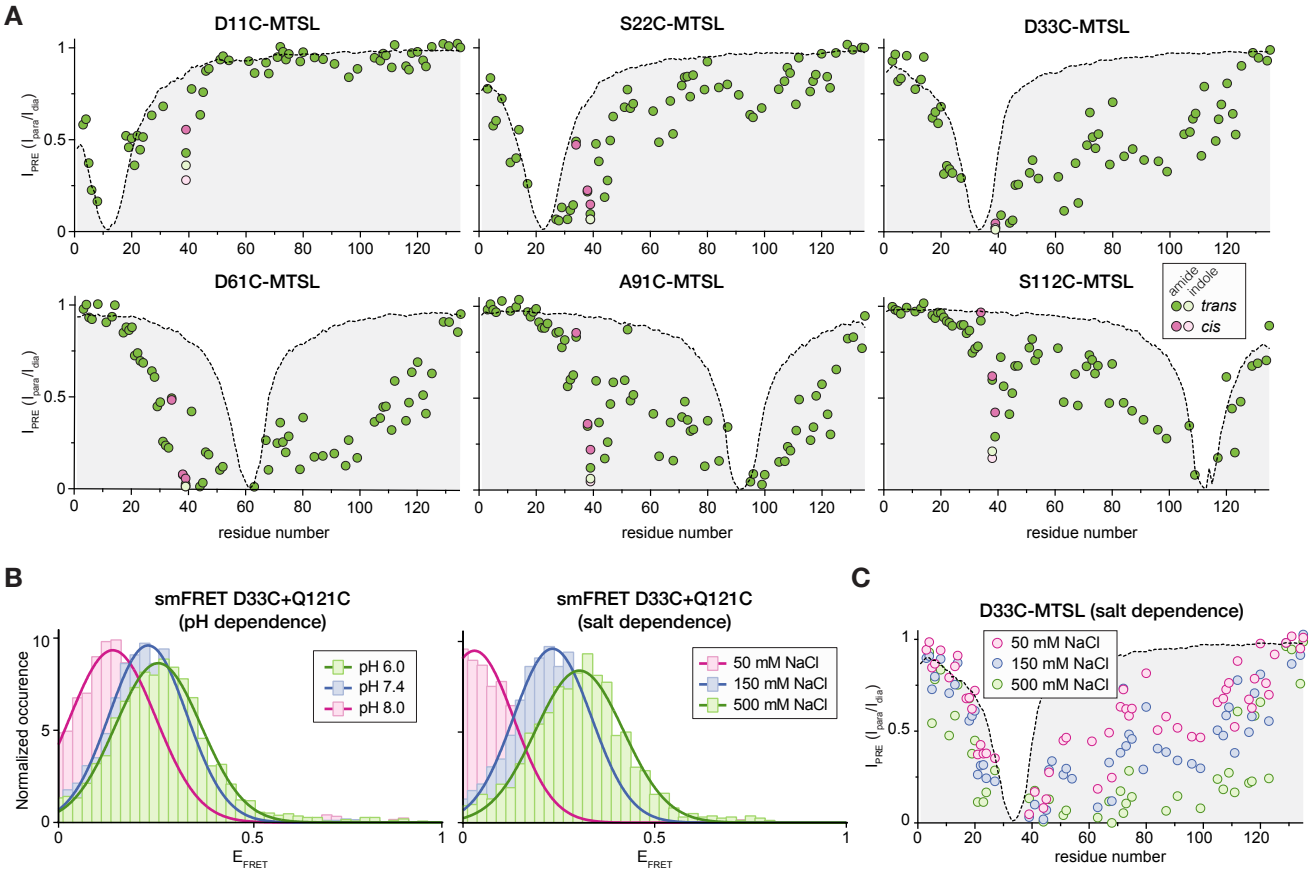

Figure 2. PRE NMR and smFRET analysis of the AF-1 structural ensemble.
(**A**) Plots of experimental IPRE values (circles) calculated from peak intensities from 2D [^{1}H,^{15}N]-HSQC NMR spectra and calculated I_{PRE} profiles (dotted line with gray shaded area) from flexible-meccano simulations of extended AF-1 conformers for MTSL-conjugated AF-1 constructs as noted.
(**B**) Two-color smFRET data of D33C+Q121C double mutant AF-1 conjugated with Alexa Fluor 488 and 647 maleimide as a function of pH (left) or salt concentration (right).
(**C**) Plot of experimental IPRE values for the D33C-MTSL AF-1 construct from 2D [^{1}H,^{15}N]-HSQC NMR spectra collected as a function of salt concentration (circles); calculated I_{PRE} profile for the extended D33C-MTSL AF-1 conformers from (A) is also shown

MTSL is placed between D33 and S112, suggesting most of the AF-1 compact conformation occurs within this region.

The sequence composition of the AF-1 shows a net negative charge (**Figure S2**) and a calculated pI of 4.17, which led us to hypothesize negative charge-charge interactions may influence the relative compactness of the AF-1 conformational ensemble. To test this, we performed smFRET using a two-color approach [33, 34] with an AF-1 double mutant construct in which cysteines were placed near the N-terminus (D33C) and C-terminus (Q121C). Increasing FRET efficiency (E_{FRET}) between the D33C and Q121C sites was observed at lower pH or increasing salt concentration (**Figure 2B**), indicating that salt neutralization of the negatively charged AF-1 side chains results in a more compact AF-1 conformation. Salt-dependent PRE NMR analysis of the AF-1 with the MTSL spin label placed at D33C validated these findings since intramolecular PREs increased with increasing salt concentration (**Figure 2C**). Taken together, the smFRET and PRE NMR data indicate the AF-1 transiently samples compact conformations that can be fine-tuned by changes in charge repulsion.

P40 influences AF-1 isomerization and inhibits transcription

While performing backbone NMR chemical shift assignment of the AF-1, we noticed a region displaying two populations of chemical shifts encompassing residues T34-N42 (^{34}TEMPFWPTN^{42}), a sequence conserved among both γ2 and γ1 isoforms and different PPARγ orthologs (**Figure 3A**). This observation indicates this region of the AF-1 slowly interconverts between two structural populations on the millisecond-to-second time scale, which can be detected using ZZ-exchange NMR methods. Only one tryptophan residue (W39) is present in the AF-1, but two tryptophan side-chain indole peaks are present with populations of ~85% and ~15% (**Figure 3B**). ZZ-exchange measurements at 25°C revealed no cross-correlated exchange for these W39 indole peaks. However, ZZ-exchange measurements at elevated temperatures revealed an increasing population of cross-correlated peaks indicating this region of the AF-1 slowly interconverts or isomerizes between at least two structural conformations on a timescale (τ_{ex}) of milliseconds/seconds at elevated temperature to seconds/minutes at lower temperatures.

Two proline residues, P37 and P40, are located within this slowly isomerizing region, which led us to hypothesize that proline *cis/trans* isomerization contributes to the mechanism. Chemical shift values of proline Cβ and Cγ nuclei are predictive of *cis* or *trans* proline conformations [35, 36]. We therefore analyzed CC(CO)NH NMR data of the AF-1 (**Figure 3C**) and found that the Cβ and Cγ chemical shifts of the two P37 conformations populate a *trans* conformation. In contrast, the two P40 conformations showed Cβ and Cγ chemical shifts consistent with one *trans* and one *cis* conformation. These data pinpoint the W39-P40 (Trp-Pro) motif, a dipeptide sequence previously shown to enrich the *cis* isomer [37], as the likely origin of the slowly isomerizing AF-1 conformational switch.

To confirm the role of *cis/trans* isomerization of P40 in populating the two long-lived AF-1 conformations, we compared 2D [^{1}H,^{15}N]-HSQC

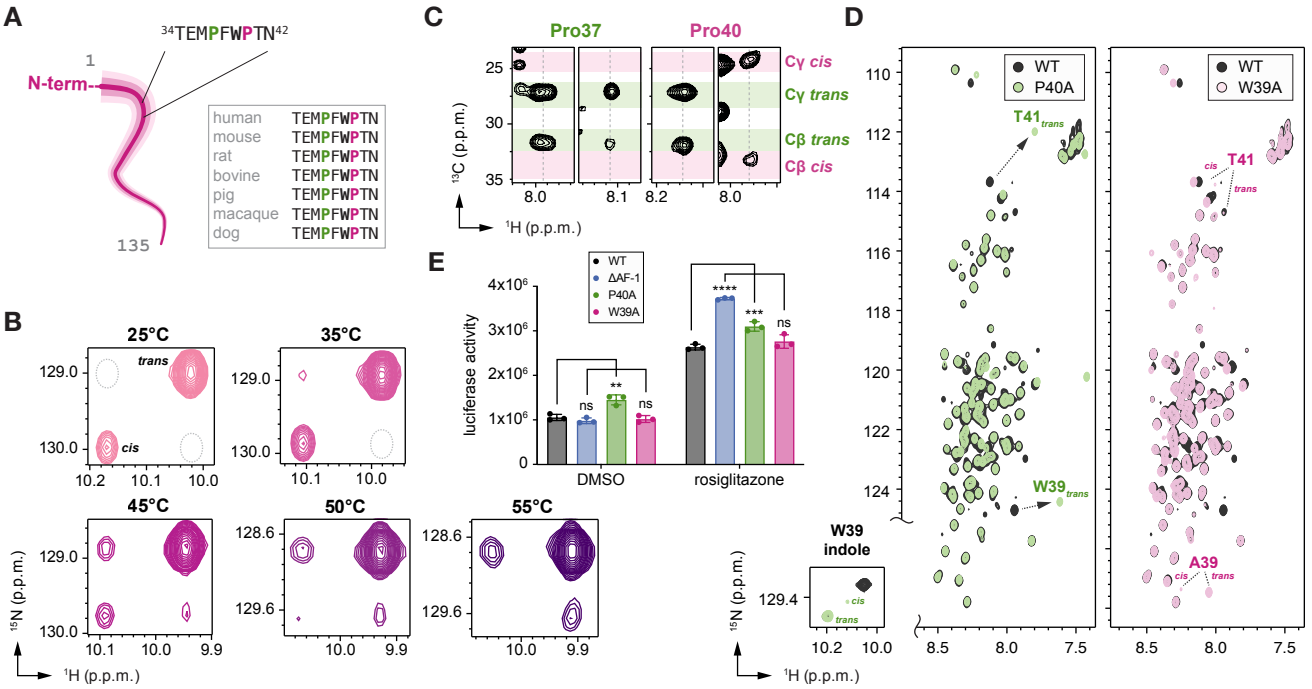

Figure 3. Proline cis/trans isomerization populates two long-lived AF-1 conformations.
(**A**) Residues within the AF-1 displaying two populations of NMR peaks localize to a region containing two proline residues (P37, green; P40, pink), one of which is adjacent to a tryptophan residue (W39).
(**B**) ZZ-exchange NMR data (delay = 2 s) focused on the W39 indole peaks shows cross-correlated peaks appearing at elevated temperatures that are missing at lower temperatures (dashed gray oval).
(**C**) Strips from 3D CC(CO)NH NMR data focused on P37 (i-1 to F38 amides) and P40 (i-1 to T41 amides). Average chemical shift ranges for *trans* and *cis* conformers of proline Cγ and Cβ atoms are displayed in green (*trans*) and pink (*cis*).
(**D**) Overlay of 2D [^{1}H,^{15}N]-HSQC NMR spectra comparing wild-type AF-1 to P40A (green) or W39A (pink) mutants.
(**E**) Cell-based luciferase reporter assay in HEK293T cells to assess the ability of full-length PPARγ and mutant constructs to activate transcription without or with treatment of the synthetic PPARγ agonist rosiglitazone (1 μM) using a 3xPPRE-luciferase reporter plasmid (n=3). Bars and error bars represent the mean and s.d.; data representative of >2 experiments.

NMR of P40A and W39A AF-1 mutants to WT AF-1 (**Figure 3D**). The P40A mutant suppresses but does not completely abolish *cis/trans* isomerization of this region, changing the relative *cis/trans* populations from ~85%/15% in WT to ~94%/6% (**Table S1**). As expected, W39 indole peaks are absent in the W39A mutant; however, *cis/trans* populations are still observed in this mutant (~89%/11%) that are more similar to WT levels, suggesting W39 may be dispensable for *cis/trans* isomerization.

To determine how the mutants impact PPARγ transcription, we performed a cell-based transcriptional reporter assay (**Figure 3E**) along with western blot analysis of protein levels (**Figure S3**). HEK293T cells were transfected with a PPAR-responsive luciferase reporter plasmid along with expression constructs encoding wild type (WT) PPARγ or mutant variants (W39A or P40A) to test the functional role of the Trp-Pro motif. We also tested a DBD-hinge-LBD construct lacking AF-1 (ΔAF-1), which was previously shown to increase PPARγ transcription in differentiated mouse adipocytes. In the absence of ligand, the P40A construct displayed an increase in transcription relative to WT PPARγ, while there was no significant effect of ΔAF-1 or W39A constructs. When HEK293T cells were treated with the synthetic PPARγ agonist rosiglitazone to mimic the condition where endogenous ligands are produced in differentiated adipocytes, the ΔAF-1 and P40A constructs displayed an increase in transcription relative to WT PPARγ, whereas the W39A mutant displayed no significant change. These findings indicate that removal of the AF-1 inhibits ligand-dependent activity, while the inhibitory effect of P40 *cis/trans* isomerization is ligand-independent. The minimal effect of the W39A mutation on *cis/trans* populations by NMR and transcription in cells suggests that W39 may be dispensible for isomerization and that isomerization may be driven by alternative mechanisms.

AF-1/LBD interdomain interaction in full-length PPARγ

To determine whether the two long-lived AF-1 conformations occur in full-length PPARγ, we compared 1D [^{1}H]-NMR spectra of AF-1 and full-length PPARγ. Focusing on the indole peaks of W39 (**Figure 4A**), which is the only tryptophan residue in PPARγ, two peaks are observed in full-length PPARγ that are shifted downfield (i.e., to the left) relative to the peaks observed in the AF-1 alone. Addition of the agonist ligand rosiglitazone, which stabilizes an active LBD conformation, shifts the full-length PPARγ W39 indole peaks further downfield, indicating that ligand binding at the LBD affects the chemical environment of the AF-1.

To extend our 1D [^{1}H]-NMR findings, we used sortase A-mediated protein ligation and segmental isotope labeling [38, 39] to generate full-length PPARγ protein where only the AF-1 is ^{15}N-labeled and visible in 2D [^{1}H,^{15}N]-HSQC NMR data. Overlay of 2D NMR spectra of segmentally [^{15}N-labeled AF-1] full-length PPARγ construct and the isolated ^{15}N-labeled AF-1 reveals select chemical shift and line broadening changes (**Figure 4B**). For example, in the full-length PPARγ data the peak corresponding to the last residue in the isolated AF-1 (M135) is not present and several other C-terminal residues show chemical shift changes, confirming the segmentally labeled sample observed for full-length PPARγ is completely ligated. The two W39 indole peaks are shifted downfield relative to the isolated AF-1 spectrum, consistent with the 1D NMR analysis of isolated AF-1 and full-length PPARγ. Furthermore, residues in AF-1 regions involved in intramolecular PRE contacts (**Figure 2**) also show chemical shift and peak line broadening changes in the differential 2D NMR data. Taken together, these findings indicate the

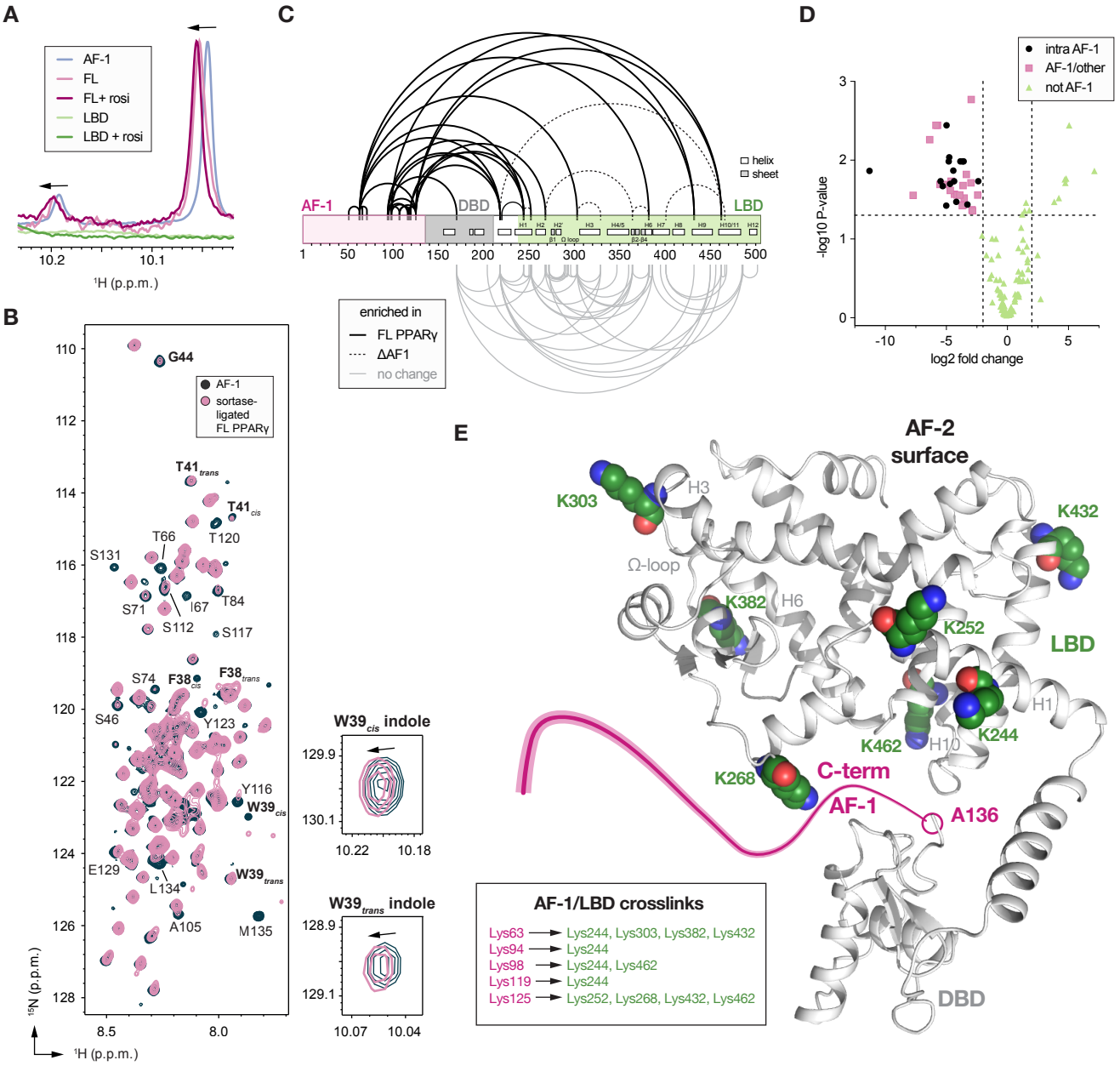

Figure 4. NMR and XL-MS reveal the AF-1 and LBD interact in full-length PPARγ.
(**A**) Overlay of 1D [¹H]-NMR spectra focused on the region containing the W39 indole peaks.
(**B**) Overlay of 2D [¹H,¹⁵N]-HSQC NMR spectra comparing AF-1 to sortase A-ligated full-length PPARγ where only the AF-1 (residues 1-135) is ¹⁵N-labeled. Residues with notable differences are annotated, and residues near the Trp-Pro (W39-P40) motif are in bold font.
(**C**) DSSO crosslinks detected in differential XL-MS analysis of full-length PPARγ vs. AF-1 truncation (ΔAF-1).
(**D**) Plot of the P-value vs. fold change of DSSO crosslinks from the differential XL-MS analysis.
(**E**) LBD residues involved in AF-1 crosslinks plotted on the AlphaFold structure of PPARγ (residues 136-505); the putative location of the AF-1, which is missing in crystal structures of full-length PPARγ, is shown in pink.

chemical environment of the AF-1 is different within the context of the full-length protein in a ligand-dependent manner. Furthermore, these data suggest there may be interdomain contacts in full-length PPARγ, such as a physical AF-1/LBD interaction, that involve regions of the AF-1 involved in intradomain contacts defined by our PRE NMR analysis.

To corroborate our NMR findings that the AF-1 and LBD physically interact in full-length PPARγ, we performed chemical crosslinking mass spectrometry (XL-MS) comparing DSSO-crosslinked samples of full-length PPARγ to a truncated construct without the AF-1 containing the DBD-hinge-LBD (ΔAF-1). The differential analysis revealed 38 crosslinks enriched in full-length PPARγ (**Figure 4C**) including 16 unique intradomain AF-1 crosslinks and 13 unique AF-1/LBD crosslinks (**Figure 4D**). Crosslinks involving the AF-1 localize primarily to the C-terminal half of the AF-1 between K94 and K125, which contains 5 out of 6 lysine residues present in the AF-1. Seven LBD residues involved in interdomain AF-1 crosslinks include residues near the β-sheet surface on helix 1 (K244, K252), helix 2 (K268), Ω-loop (K303), helix 6 (K382), and helix 10 (K462)—as well as a lysine residue near the AF-2 surface (K432). These LBD crosslinks are consistent with the putative location of the AF-1 region in the crystal structure of full-length PPARγ where electron density for the AF-1 was not observed (**Figure 4E**) [11]. Furthermore, 7 crosslinks are enriched in ΔAF-1 PPARγ, of which 6 are LBD/LBD

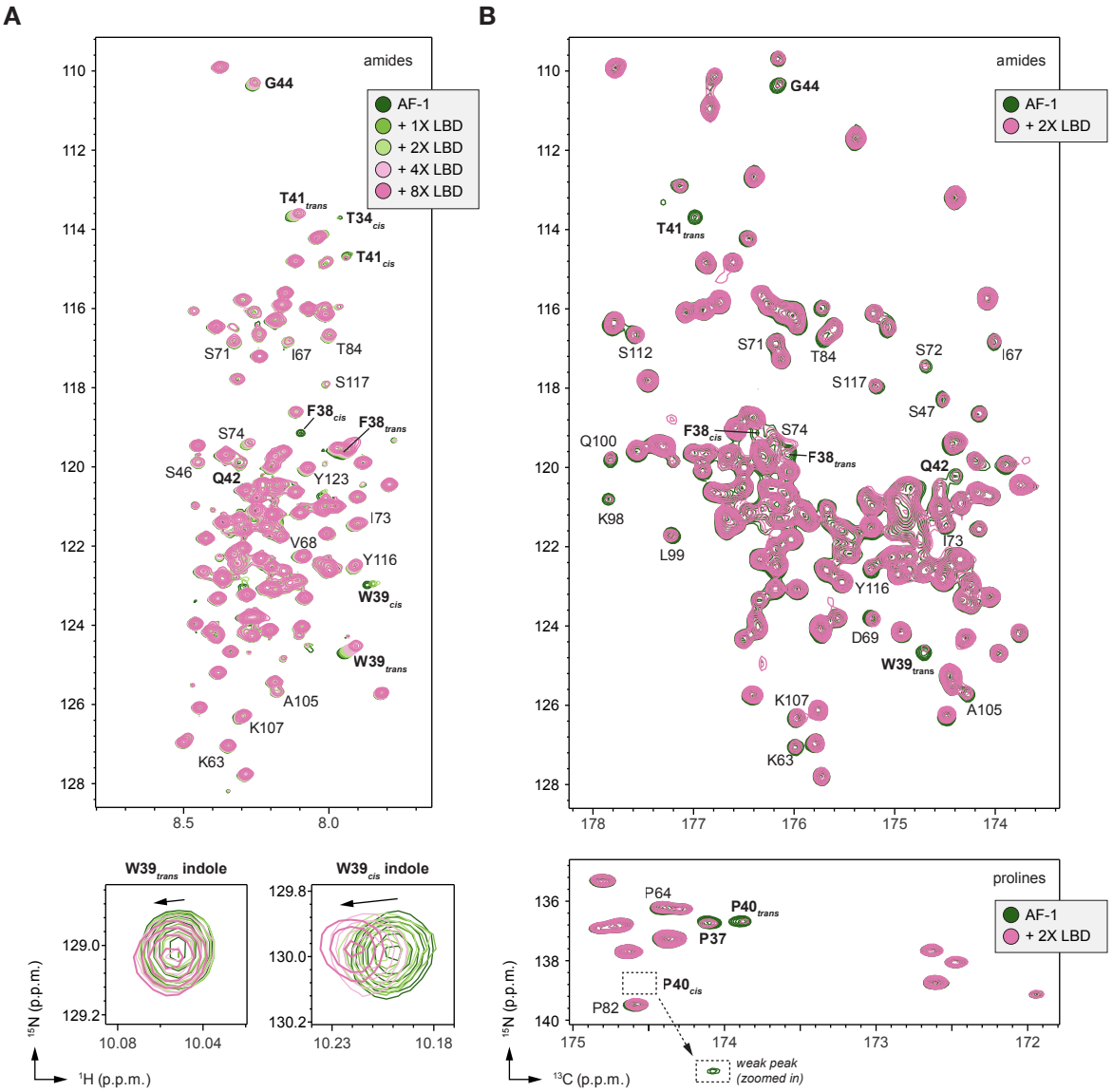

Figure 5. NMR structural footprinting of LBD binding regions within the AF-1.
(**A**) Overlay of 2D [^{1}H,^{15}N]-HSQC NMR spectra of ^{15}N-labeled AF-1 with increasing concentrations of LBD. Residues with notable differences are annotated, and residues near the Trp-Pro (W39-P40) motif are in bold font.
(**B**) Overlay of 2D [^{13}C,^{15}N]-(HACA)CON NMR spectra of ^{13}C,^{15}N-labeled AF-1 containing an N-terminal 6xHis+TEV tag with or without LBD. Residues with notable differences are annotated, and residues near the Trp-Pro (W39-P40) motif are in bold font.

crosslinks that also localize near the β-sheet surface—indicating the AF-1, and by corollary its removal, structurally affects the LBD conformation.

Trp-Pro motif is a major determinant in LBD interaction

The XL-MS data of full-length PPARγ, though limited to detecting interactions to the C-terminal half of the AF-1, show this region interacts with the β-sheet LBD surface. However, the differential AF-1 vs. sortase-ligated full-length NMR data suggest a more extensive interaction involving other regions of the AF-1. We therefore performed NMR chemical shift structural footprinting analysis to more completely map the interaction between the isolated AF-1 and LBD. To map the LBD-binding interface within the AF-1, we collected 2D [^{1}H,^{15}N]-HSQC data (**Figure 5A**) and 2D [^{13}C,^{15}N]-(HACA)CON data (**Figure 5B**) of ^{15}N- or ^{13}C,^{15}N-labeled AF-1, respectively, in the absence and presence of LBD. Addition of LBD caused changes in AF-1 chemical shifts (fast exchange on the NMR time scale) and peak line broadening (intermediate exchange on the NMR time scale) for select residues, confirming a direct interaction between the isolated domains. There are three notable features apparent in these NMR structural footprinting data.

First, AF-1 residues most affected that display the largest chemical shift changes and peak line broadening include F38, W39, P40, and T41—pinpointing the slowly exchanging Trp-Pro motif as a major determinant in the LBD interaction. Similar to the 1D and 2D differential NMR data of full-length PPARγ and sortase-ligated full-length PPARγ, the W39 indole side chain peaks are shifted downfield with increasing LBD concentrations. Furthermore, chemical shift perturbations or peak movements for other backbone amide residues occur in a similar direction between the isolated AF-1/LBD titration data and the differential sortase full-length NMR data. These observations indicate the interaction between the isolated AF-1 and LBD interaction is similar to what occurs within the context of full-length PPARγ.

Second, AF-1 residues distal in primary sequence from the Trp-Pro motif show chemical shift perturbations in the NMR structural footprinting data and correspond to regions involved in intramolecular PRE contacts to the Trp-Pro region. Chemical shift changes and peak

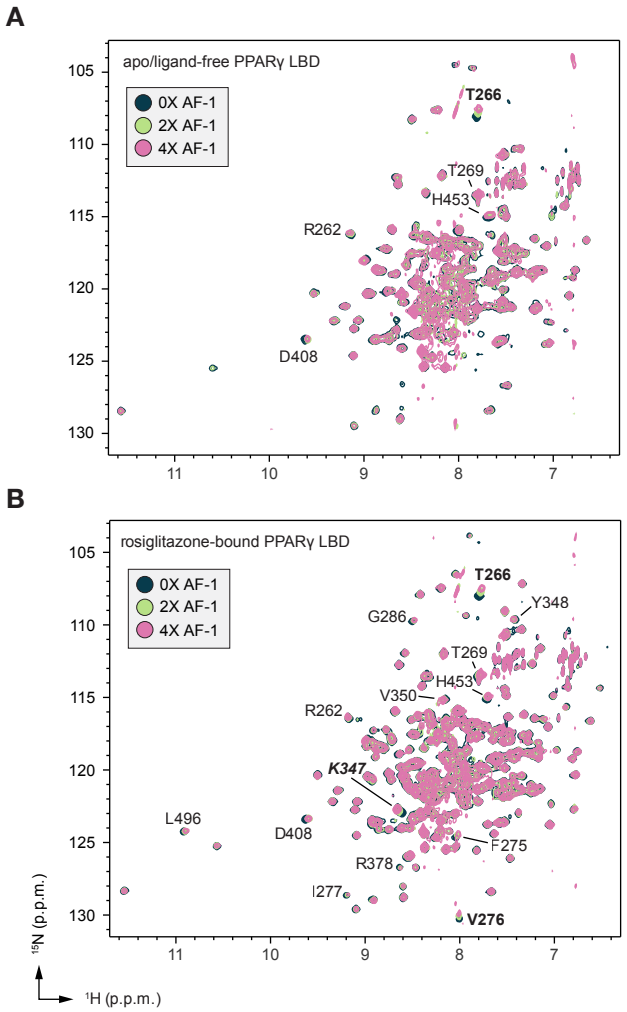

Figure 6. NMR structural footprinting of AF-1 binding regions within the LBD.
(**A**,**B**) Overlay of 2D [^{1}H,^{15}N]-TROSY-HSQC NMR spectra of ^{15}N-labeled apo-LBD (**A**) or ^{15}N-labeled rosiglitazone-bound LBD (**B**) with increasing concentrations of AF-1. Residues with notable differences are annotated, and residues with the largest changes are in bold font.

line broadening is also observed for these residues in the 2D differential sortase NMR data on full-length PPARγ vs. isolated AF-1. These observations suggest a more extensive LBD interaction interface or allosteric conformational changes that occur in the AF-1 upon LBD interaction.

Third, in the 2D [^{1}H,^{15}N]-HSQC data, increasing LBD concentrations causes a chemical shift change in the *trans* conformation of the Trp-Pro region characterized primarily by fast exchange on the NMR time scale, whereas the *cis* conformation displays a combination of notable intermediate exchange (peak disappearance) and fast exchange. This difference in exchange on the NMR time scale suggests that the *cis* AF-1 conformation may interact with the LBD with higher affinity and/or different interaction kinetics than the *trans* AF-1 conformation.

Trp-Pro AF-1 motif interacts with two LBD surfaces: the β-sheet and AF-2

To map the AF-1-binding interface within the LBD, we collected 2D [^{1}H,^{15}N]-TROSY-HSQC data of ^{15}N-labeled PPARγ LBD in the absence and presence of AF-1. Apo/ligand-free PPARγ LBD dynamically exchanges between transcriptionally active and repressive conformations on the intermediate exchange NMR time scale resulting in missing or very broad peaks for about half of the LBD including residues within and near the orthosteric ligand-binding pocket and AF-2 surface [6, 28] due to dynamic exchange between active and repressive LBD conformations [8]. Upon binding a full agonist such as rosiglitazone, which stabilizes an active LBD conformation, nearly all NMR peaks are visible [6, 8]. We therefore performed studies in the apo-LBD form and in the presence of rosiglitazone to fully map the AF-1 interaction surface on the LBD. Titration of AF-1 into ^{15}N-labeled apo-LBD revealed chemical shift perturbations for several NMR peaks (**Figure 6A**). Residues that show the largest chemical shift changes colocalize near the β-sheet surface and include R262, T266, and T269 on helix 2; D408 on the helix 7-8 loop; and H453 on the helix 9-10 loop. To obtain a more holistic view of the AF-1 binding surface, we titrated AF-1 into ^{15}N-labeled LBD bound to rosiglitazone and observed additional chemical shift perturbations in regions that are stabilized in the active conformation (**Figure 6B**). Agonist-stabilized residues that show the largest chemical shift changes include additional residues on the β-sheet surface (F275, V276, I277, G286, R378); as well as residues within the AF-2 coregulator interaction surface (K347, Y348, and V350 on helix 5; and L496 on helix 12).

NMR chemical shift footprinting analysis reports on both residues directly involved in the AF-1/LBD interaction as well as allosteric conformational changes that occur upon binding. We therefore performed intermolecular PRE NMR to specifically map where the AF-1 region containing the Trp-Pro motif interacts on the LBD. We collected 2D [^{1}H,^{15}N]-TROSY-HSQC data of ^{15}N-labeled LBD bound to rosiglitazone in the presence of AF-1 with a MTSL spin label placed at D33 (D33C-MTSL) near the Trp-Pro motif (**Figure 7A**). Differential analysis of AF-1 D33C-MTSL in the paramagnetic and diamagnetic states showed decreases in NMR peak intensity (**Figure 7B**) for residues at two distinct LBD surfaces (**Figure 7C**): a large grouping of residues comprising the AF-2 coregulator interaction surface, and a smaller grouping of residues near the β-sheet surface.

To confirm the AF-2 surface interaction with the Trp-Pro motif, we took advantage of a double mutant LBD construct we previously generated (C313A/K502C) where we introduced a cysteine residue on the AF-2 surface within helix 12 (K502C) and removed the only cysteine residue in the LBD (C313A) to enable site-specific covalent labeling to the AF-2 helix 12 [8, 40, 41]. Using this construct, we performed intermolecular PRE NMR with ^{15}N-labeled AF-1 in the presence of K502C-MTSL LBD. Differential analysis with apo K502C-MTSL LBD revealed the largest decrease in I_{PRE} values within and near the Trp-Pro motif though some smaller PRE effects are also observed where the I_{PRE} values dip below 0.9 for residues within regions involved in intradomain AF-1 contacts (**Figure 7D**). In the presence of rosiglitazone-bound K502C-MTSL LBD, compared to apo K502C-MTSL LBD, a larger decrease in peak intensity is observed for the W39 *trans* indole conformation but not the *cis* conformation (**Figure 7E**). This could indicate an interaction preference with the Trp-Pro motif in the *trans* AF-1 conformation for agonist-stabilized active LBD conformation.

Taken together, the intermolecular PRE data corroborate the NMR structural footprinting data and extend the XL-MS data revealing that both the β-sheet and AF-2 LBD surfaces are involved in the AF-1 interaction. Furthermore, our studies pinpoint the slowly exchanging AF-1 Trp-Pro motif, which populates two long-lived AF-1 structural conformations, as a major interaction determinant with the AF-2 coregulator interaction surface in the LBD.

DISCUSSION

The disordered N-terminal PPARγ AF-1 domain is an important regulator of PPARγ function. Previous studies have indicated the AF-1 negatively regulates PPARγ transcription and PPARγ-mediated adipogenesis via an AF-1/LBD interdomain functional communication

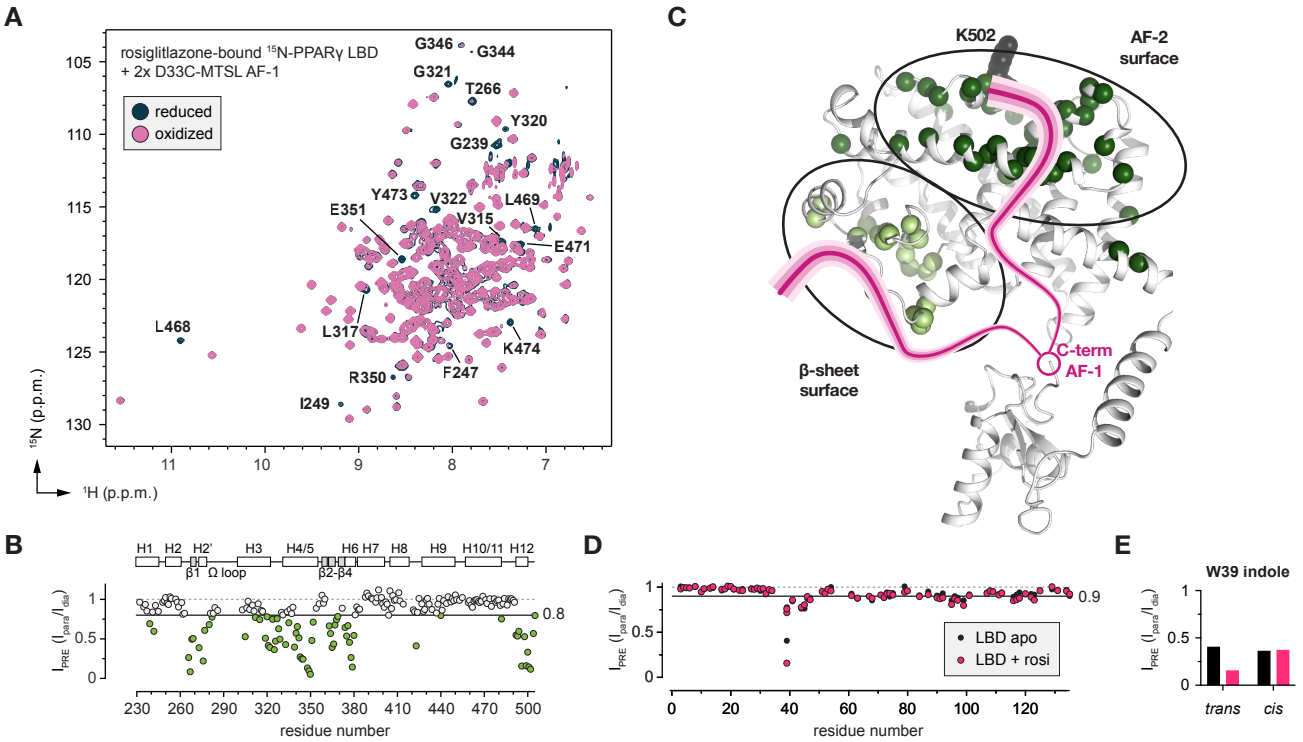

Figure 7. PRE NMR analysis reveals the AF-1 Trp-Pro motif interacts with two LBD surfaces. (**A**) Overlay of 2D [^{1}H,^{15}N]-TROSY-HSQC PRE NMR spectra of ^{15}N-labeled rosiglitazone-bound LBD with 2x D33C-MTSL AF-1 in the paramagnetic (oxidized) and diamagnetic (reduced) states. Residues with notable differences are annotated. (**B**) Plot of I_{PRE} values calculated from the PRE NMR spectra in (A) vs. residue number. Secondary structural elements of the LBD are shown above the plot. (**C**) LBD residues with I_{PRE} values ≤ 0.8 in (B) displayed on the AlphaFold structure of PPARγ (residues 136-505) map to two distinct surfaces (light vs. dark spheres; black circles); the putative location of the AF-1, which is missing in crystal structures of full-length PPARγ, is shown in pink. (**D,E**) Plot of backbone amide (**D**) and W39 indole (**E**) I_{PRE} values calculated from the PRE NMR spectra of ^{15}N-labeled AF1 with 2x K502C-MTSL LBD vs. residue number.

mechanism [19–23]. However, the structural basis for AF-1 activity, including its effects on the LBD, has remained elusive due to its disordered properties that make it difficult to study by X-ray crystallography or cryo-EM. Here, we used a combination of solution-based techniques to characterize the structural properties of the PPARγ AF-1. We found that although predominantly disordered, the AF-1 is characterized by transient long-range intramolecular contacts that can be enhanced by decreasing negative charge repulsion. Thus, a change in AF-1 structure and compaction could occur under cellular states that would affect protein net charge, such as the presence of binding partners including other proteins, nucleic acids (mRNA and chromatin), or small molecule metabolites [1]; upon post-translational modification of PPARγ [42]; or cellular compartments with localized changes in ionic strength or pH such as phase separated biomolecular condensates [43].

Our NMR analysis also revealed that the AF-1 contains an evolutionarily conserved Trp-Pro motif that undergoes *cis/trans* isomerization on a slow timescale (milliseconds to seconds) populating two long-lived AF-1 conformations. Tryptophan is known to facilitate isomerization of neighboring proline residues [37]; however the W39A mutant failed to fully disrupt isomerization and there was some residual isomerization even in the P40A mutant. Residues preceding the Trp-Pro motif, including P37 and F38, may also contribute to isomerization of this region. The strong propensity for isomerization despite these mutations suggests it is a robust dynamic property of this region, and the observation that the P40A mutation increases cell-based transcriptional activity of PPARγ indicates isomerization of this region may have important cellular functions that warrants further study.

Previous studies showed the AF-1 inhibits ligand-dependent PPARγ activity, but did not determine whether the effects were due to a direct AF-1/LBD interaction [19–23]. However, AF-1/NTD interactions with nuclear receptor LBDs have been reported or suggested for at least four other nuclear receptors including androgen receptor [44–51], estrogen receptor [52,53], glucocorticoid receptor [54], and mineralocorticoid receptor [55,56]. Using CSP and PRE NMR, we tested for AF-1/LBD binding and found the AF-1 contacts the LBD at two distinct surfaces. Unlike the AF-1/AF-2 interaction identified for androgen receptor, in which an FXXLF motif within the AF-1 folds upon binding, the "fuzzy" interaction observed for PPARγ aligns with others previously identified for disordered proteins [57, 58]. Intriguingly, our results indicate the AF-2 surface of the LBD predominantly interacts with the region encompassing the AF-1 Trp-Pro motif, which notably is present in both major PPARγ isoforms (γ1 and γ2). Although our NMR data suggest the interaction may be somewhat weak when the isolated AF-1 and LBD are titrated together, given the chemical shift perturbations occur on the fast-to-intermediate NMR time scale, within the context of full-length PPARγ the interaction is likely to be more robust since the two domains are physically tethered together joined by the DBD and hinge region.

Previous studies indicated the AF-1 inhibits PPARγ function such that AF-1 deletion results in increased PPARγ transcription in differentiated mouse adipocytes [19]. Our experiments using human HEK293 cells revealed the inhibitory effect of the AF-1 on PPARγ transcription was only evident in the presence of an activating PPARγ ligand. Although the prior study did not add a PPARγ ligand, mouse adipocytes are known to produce activating PPARγ ligands naturally during adipogenesis [59]. Thus, it will be important to explore how AF-1 binding to the LBD inhibits ligand binding or affects coregulator binding at the AF-2 surface. Given our data that the AF-1 interacts with the AF-2 surface, the AF-1 could directly compete for coactivator binding as previously observed for the

AR and ER AF-1 [51, 53], which would explain why AF-1 deletion increases PPARγ transcription. Likewise, AF-1 interactions at the LBD β-sheet surface could interfere with ligand exchange into the orthosteric ligand-binding pocket [4], conformational changes associated with ligand binding, or interaction with other nuclear receptors [11] or other proteins.

Proline *cis/trans* isomerization plays important roles in protein folding [60] and in the function of proteins with examples including isomerization-regulated ligand-gated ion channel pore opening [61] and isomerization within a linker region that controls interdomain autoinhibitory interactions [62–64]. More recently, studies have revealed functional regulatory roles for proline *cis/trans* isomerization in IDPs including regulation of protein-protein interactions [65, 66], conformation-specific phosphatase enzymatic activity towards phosphorylated serine-proline motifs [67], misfolding/aggregation of IDPs [68], and circadian transcriptional regulation [69]. Our discovery of the PPARγ AF-1 Trp-Pro motif interaction with the AF-2/LBD is, to our knowledge, a unique example of a disordered domain undergoing *cis/trans* isomerization that participates in an interdomain interaction with a structured domain. Since the LBD interaction occurs at the site of AF-1 *cis/trans* isomerization, it will be important in future studies to determine if AF-1 isomerization influences LBD binding and activity. Given our NMR data, which indicate the LBD interaction with the *cis* and *trans* AF-1 conformations may occur with different kinetic exchange properties and the LBD may preferentially interact with the *trans* isomer in the presence of activating ligand, changes to the isomerization rate or relative isomer populations (i.e., by an isomerase enzyme) could also modulate the AF-1/LBD interaction.

In addition to characterizing a direct interdomain interaction between the PPARγ AF-1 and LBD, our solution-based structural approach illuminates a platform to interrogate the activities of disordered nuclear receptor domains. While nearly all of the 48 human nuclear receptors contain unstructured AF-1 regions with important documented functional roles, the structural basis for their activities remain largely unexplored. Thus, it will be important to apply structural approaches such as those outlined here to gain a more comprehensive understanding of nuclear receptor activity.

MATERIALS AND METHODS

Plasmids and reagents

All plasmids and constructs use PPARγ 2 isoform numbering. For bacterial expression of proteins, DNA sequences encoding PPARγ AF-1 domain (residues 1-135), PPARγ LBD (residues 231-505), full-length PPARγ (residues 1-505), and PPARγ ΔAF-1 (residues 136-505) were inserted into pET45 or pET46 plasmids as tobacco etch virus (TEV) protease-cleavable N-terminal hexahistidine (6xHis) tag fusion proteins. Plasmids for in vitro sortase A-mediated protein ligation were generated using a published protocol [38]; the N-terminal sortase A construct contained the AF-1 (residues 1-135) along with a 5-residue extension containing the sortase A consensus sequence (LPITG) followed by a 6xHis-tag; the C-terminal construct contained a TEV-cleavable N-terminal 6xHistag followed by the PPARγ DBD-hinge-LBD (residues 136-505), which upon TEV cleavage leaves an N-terminal Gly residue required for sortase A ligation. For mammalian cellular studies, plasmids including full-length PPARγ isoform 2 (residues 1-505) and tk-LUC 3xPRE luciferase reporter were previously reported [70]. Mutant constructs were generated using site directed mutagenesis using PfuUltra II high fidelity polymerase (Agilent) and following manufacturer's protocol. All plasmids were confirmed by Sanger sequencing (Genewiz) prior to use.

Protein expression and purification

Proteins were expressed in *Escherichia coli* BL21(DE3) cells (Life Technologies). Full-length and ΔAF-1 PPARγ proteins were expressed using an autoinduction procedure where cells were grown for 6 hrs at 37 ˚C followed by addition of 0.1 mM zinc chloride, temperature reduction to 22 ˚C for 16 hrs. PPARγ AF-1, LBD, and sortase A-compatible proteins were either expressed in Terrific Broth (TB) media or M9 media supplemented with ^{13}C-glucose and/or $^{15}NH_4Cl$ (Cambridge Isotope Labs, Inc.) followed by protein induction with 0.5 mM isopropyl ß-D-1-thiogalactopyranoside (Gold Biotechnology) at 18˚C for 16 hrs. Cells were harvested by centrifugation, washed with phosphate buffered saline (PBS) buffer, and resuspended in a cell lysis buffer containing 40 mM potassium phosphate (pH 7.4), 500 mM potassium chloride, 15 mM imidazole, 0.5mM ethylenediaminetetraacetic acid (EDTA), 1 mM phenylmethylsulfonyl fluoride (PMSF), and Pierce protease inhibitor tablets (Thermo Scientific). Cells were lysed by sonication and the lysate was clarified by centrifugation at 14000 rpm for 45 min and filtered with a 0.2μm filter prior to loading into the Ni-NTA column. The protein was eluted against a 500 mM imidazole gradient through a Ni-NTA column, followed by overnight dialysis against a buffer without imidazole for TEV protease His tag cleavage at 4°C. The next morning, the sample was loaded onto the Ni-NTA column for contaminant and tag removal. The flow through containing the purified protein was collected, concentrated, and ran through an S75 size exclusion column (GE healthcare) in the NMR buffer (20 mM KPO_4 pH 7.4, 50 mM KCl, and 0.5 mM EDTA. For PPARγ full-length and LBD the corresponding protein peak was collected and stored at -80 ˚C prior to use. For PPARγ AF1 the corresponding protein peak was collected, concentrated to 5mL and boiled at 70˚C for 10 min. The sample was centrifuged at 4000 rpm for 15 min, filtered with a 0.2μm filter and loaded into a Q column (GE healthcare) to remove suspected lingering proteases and DnaK. The column was eluted with a 1M potassium chloride gradient where the most prominent peak corresponds to our protein of interest. The peak was collected and dialysed overnight in the NMR buffer. The next day, the protein was concentrated and stored at -80˚C. All purified proteins were verified by SDS-PAGE as >95% pure and 1mM TCEP was added to all the buffers during PPARγ full-length purification.

CD spectroscopy

Circular dichroism (CD) data of PPARγ AF-1 and LBD were collected using a Jasco J-815 CD Spectropolarimeter using a buffer containing 10 mM potassium phosphate and 50 mM potassium fluoride. An average of 3 scans were recorded per measurement using a scan speed of 100 nm/min at room temperature (~23 ˚C) between a spectral range of 190-260 nm using a 1-mm optical bandwidth. Thermal unfolding curves were obtained by increasing the temperature from 0-00 ˚C with measurements recorded at 222 nm and 200 nm.

Sortase A-mediated protein ligation

Purified Sortase 4M enzyme was obtained from A. Byrd lab (NIH) [38] and used to ligate ^{15}N-labeled AF-1(residues 1-135)+LPITG+6xHis-tag protein (60 μM final concentration) to unlabeled Gly-DBD-hinge-LBD (residues 136-505; 60 μM final concentration). The ligation was performed in a buffer containing 50 mM TrisHCl (pH 7.8), 5 mM $CaCl_2$, 100 mM NaCl, 0.2 mM TCEP, and 5 μM Sortase4M (final concentration). After 30 min, the ligation product (full-length PPARγ containing an LPITG insert between the 15N-labeled AF-1 and unlabeled DBD-hinge-LBD) was purified using a HisTrapFF column washed with a buffer containing 40 mM phosphate buffer (pH 7.4), 500 mM KCl, 15 mM imidazole, and 1 mM TCEP and eluted in a similar buffer containing 500 mM imidazole. To remove the 6xHis-tag, TEV protease was added to the ligated sample and incubated overnight at 4 ˚C in a buffer containing 40 mM potassium phosphate (pH 7.4), 200 mM KCl, 0.5 mM EDTA, and 1 mM TCEP. Protein was reloaded onto the HisTrapFF column and the unbound fraction was collected and concentrated with a 30 kDa Amicon concentrator to 11.6 mg/mL (200 μM).

MTSL nitroxide spin labeling for PRE NMR studies

MTSL labeling of proteins was performed following a published protocol [31]. Briefly, proteins were concentrated to ~300-500 μM in 1 mL, reduced with 1.25 mM dithiothreitol (DTT), and passed through a Zeba desalting column (Thermo Scientific) that had been equilibrated with NMR buffer; the eluate was collected, wrapped in aluminum foil, and supplemented with NMR buffer containing 10 molar equivalents of MTSL (Cayman Chemical #16463; also called MTSSL)from a stock solution in 100% DMSO-d_6. The labeling reaction was set up at room temperature (~23 ˚C) for 15 min with gentle mixing followed by an overnight (~18 hrs) incubation after addition of another 10 molar equivalents of MTSL. The following day, the MTSL-labeled protein was concentrated to 400 μL and dialysed for 16 hrs at 4 ˚C in the dark to remove unconjugated MTSL.

NMR spectroscopy

NMR experiments were acquired at 298 K (unless indicated otherwise) on a Bruker 700 MHz NMR instrument equipped with a QCI-P cryoprobe or a Bruker 600 MHz NMR instrument equipped with a TCI-H/F cryoprobe. NMR samples were prepared in NMR buffer (50 mM potassium phosphate, 20 mM potassium chloride, 1 mM TCEP, pH 7.4, 10% D_2O) and typically contained 100-600 μM of the isotopically labeled component (^{13}C and/or ^{15}N); no significant chemical shift differences were observed within this concentration range. 3D NMR experiments used for AF-1 chemical shift assignment were collected using a 300 μM ^{13}C,^{15}N-labeled AF-1 sample with an N-terminal 6xHis+TEV tag and included HNCO, HN(CO)CA, CBCANH, CBCA(CO)NH, and CC(CO)NH. 2D NMR experiments included 2D [^{1}H,^{15}N]-HSQC, 2D [^{13}C,^{15}N]-(HACA)CON [71], and ZZ-exchange measurements via 2D [^{1}H,^{15}N]-HSQC for the AF-1 at different temperatures; and [^{1}H,^{15}N]-TROSY-HSQC of the LBD with or without 2 molar equivalents of rosiglitazone (Cayman Chemical #71740). 1D [^{1}H]-NMR spectra were collected using natural abundance proteins that were not isotopically labeled. 3D [^{1}H,^{15}N,^{1}H]-NOESY-HSQC and [^{1}H,^{15}N,^{1}H]-TOCSY-HSQC experiments were used to aid in the transfer WT AF-1 assignments to W39A and P40A mutants using the minimal chemical shift perturbation method [72] and residue-specific chemical shift trends from the BioMagResBank (BMRB) [73]. Titration experiments for 2D NMR chemical shift structural footprinting were performed using 100 or 200 μM of the isotopically labeled component and the indicated equivalent of unlabeled component. PRE NMR experiments were collected in the absence or presence of 5x molar excess of sodium ascorbate to reduce the MTSL nitroxide spin label; I_{PRE} values were calculated from the ratio of peak intensities (I_{para}/I_{dia}) as previously described [31]. NMR data were collected using Bruker Topspin (v3.2) software, and processed/analyzed using NMRFx and NMRViewJ [74, 75].

DSSO chemical crosslinking of protein samples

Full-length PPARγ and PPARγ ΔAF-1 (residues 136-505) were diluted to 10 μM in a buffer containing 20 mM potassium phosphate (pH 8.0), 150 mM KCl, 0.5 mM sodium citrate, and 10% glycerol. DSSO crosslinker (ThermoFisher #A33545) was freshly dissolved in DMSO to a final concentration of 75 mM and added to the protein solution at a final concentration of 1.5 mM. The reaction was incubated at 25 °C for 1 hr and then quenched by adding Tris buffer (pH 8.0) to a final concentration of 50 mM and incubating an additional 10 min at 25 °C. Control reactions were performed in parallel without adding the DSSO crosslinker. All crosslinking reactions were carried out in three replicates. Crosslinked samples were confirmed by SDS-PAGE and Coomassie staining along with negative control samples that were not treated with DSSO. Samples were separately pooled, precipitated using acetone, and dried protein pellets were resuspended to 12.5 μL in a buffer containing 50 mM ammonium bicarbonate (pH 8.0) and 8 M urea. ProteaseMAX (Promega, V5111) was added to the resuspended samples to a final concentration of 0.03%, the solutions were mixed on an orbital shaker operating at 1000 rpm for 15 min, and then 87.5 μL of 50 mM ammonium bicarbonate (pH 8.0) was added. Samples were digested for 4.5 hrs using trypsin added at a ratio of 1:170 (w/w trypsin:protein) at 37 °C then subsequently digested for 18 hrs using chymotrypsin at a ratio of 1:85 (w/w chymotrypsin:protein) at 25 °C. The resulting peptides were acidified to 0.67% trifluoroacetic acid (TFA) and then desalted using C18ZipTip (Millipore cat no. ZTC18 5096). Dried peptides were frozen, stored at -20°C, and resuspended in 10 μL of 0.1% TFA in water prior to LC-MS analysis.

Chemical crosslinking mass spectrometry (XL-MS)

500 ng of sample was injected (triplicate injections for both control and crosslinked samples) onto an UltiMate 3000 UHP liquid chromatography system (Dionex, ThermoFisher). Peptides were trapped using a μPAC C18 trapping column (PharmaFluidics) using a load pump operating at 20 μL/min. Peptides were separated on a 200 cm μPAC C18 column (PharmaFluidics) using the following gradient: 5% Solvent B for 70 min, 30% Solvent B from 70 to 90 min, 55% Solvent B from 90 to 112 min, 97% Solvent B from 112 to 122 min, and 5% Solvent B from 120 to 140 min, at a flow rate of 800 nL/min. Gradient Solvent A contained 0.1% formic acid, and Solvent B contained 80% acetonitrile and 0.1% formic acid. Liquid chromatography eluate was interfaced to an Orbitrap Fusion Lumos Tribrid mass spectrometer (ThermoFisher) through a Nanospray Flex ion source (ThermoFisher). The source voltage was set to 2.5 kV, and the S-Lens RF level was set to 30%. Crosslinks were identified using a previously described MS2-MS3 method with slight modifications [76]. Full scans were recorded from m/z 350 to 1,500 at a resolution of 60,000 in the Orbitrap mass analyzer. The AGC target value was set to 4×10^5, and the maximum injection time was set to 50 ms in the Orbitrap. MS2 scans were recorded at a resolution of 30,000 in the Orbitrap mass analyzer. Only precursors with a charge state between 3 and 8 were selected for MS2 scans. The AGC target was set to 5×10^4, a maximum injection time of 54 ms, and an isolation width of 1.6 m/z. The CID fragmentation energy was set to 25%. The two most abundant reporter doublets from the MS2 scans with a charge state of 2–6, a 31.9721 Da mass difference [77], and a mass tolerance of ±10 ppm were selected for MS3. The MS3 scans were recorded in the ion trap in rapid mode using HCD fragmentation with 35% collision energy. The AGC target was set to 20,000, and the maximum injection time was set for 150 ms and the isolation width to 2.0 m/z.

To identify crosslinked peptides, Thermo .Raw files were imported into Proteome Discoverer 2.5 (ThermoFisher) and analyzed via the XlinkX algorithm [78] using the MS2_MS3 workflow with the following parameters: MS1 mass tolerance, 10 ppm; MS2 mass tolerance, 20 ppm; MS3 mass tolerance, 0.6 Da; digestion, trypsin-chymotrypsin with ten missed cleavages allowed; minimum peptide length of five amino acids; and DSSO (K, S, T, Y). The XlinkX/PD Validator node was used for crosslinked peptide validation with a 5% false discovery rate (FDR). Identified crosslinks were further validated and quantified using Skyline (version 21.1) [79] using a previously described protocol [80]. Crosslink spectral matches found in Proteome Discoverer were exported and converted to the sequence spectrum list format using Excel (Microsoft). Crosslink peak areas were assessed using the MS1 full-scan filtering protocol for peaks within 10 min of the crosslink spectral match identification. Peak areas were assigned to the specified crosslinked peptide identification if the mass error was within 10 ppm of the theoretical mass, if the isotope dot product was greater than 0.9, and if the peak was not found in the non-crosslinked negative control samples. The isotope dot product compares the distribution of the measured MS1 signals against the theoretical isotope abundance distribution calculated based on the peptide sequence. Its value ranges between 0 and 1, where 1 indicates a perfect match [81]. Pairwise comparisons were made using the "MSstats" package [82] implemented in Skyline to calculate relative fold changes and significance. Significant change thresholds were defined as a log2 fold change ± 2 and -log10 p-value greater than 1.3 (i.e., a p-value less than 0.05). The visualization of proteins and crosslinks was generated

using xiNET [83].

Fluorescent labeling of protein samples for smFRET

Purified PPARγ AF-1 D33C+Q121C mutant protein at 50 μM was labeled with Alexa Fluor 488 and Alexa Fluor 647 maleimide dyes (Thermo Fisher) in 20 mM sodium phosphate pH 7.2, 50 mM NaCl, 1 mM TCEP using a 5 mM dye stock. Six substoichiometric additions of the dyes were made to the protein construct over 3 hrs for a final three-fold molar excess of each dye vs protein. The labeled sample was passed twice through Zeba desalting columns (Thermo Scientific) equilibrated in the same buffer to remove excess fluorophores.

Single-molecule FRET (smFRET)

smFRET was performed using a two-color approach with a confocal setup where fluorescently labeled proteins diffuse freely. To record smFRET data, the labeled protein at 15 μM was diluted 100,000-fold into the buffer (10 mM sodium phosphate with specified pH values and NaCl concentrations) reaching a final concentration of approximately 150 pM. 300 μL of the diluted sample were deposited into Tween-20-coated (10% Tween 20, Sigma) coverslips (Nunc Lab-Tek Chambered Coverglass, Thermo Fisher Scientific). Background samples were prepared similarly but without protein. Fluorescence bursts were recorded over 3 hrs at 22 °C on a homebuilt multiparameter fluorescence detection microscope with pulsed interleaved excitation (MFD-PIE) as established elsewhere with minor modifications [33]. Emission from a pulsed 483-nm laser diode (LDH-D-C-485, PicoQuant) was cleaned up (Semrock, FF01-482/25-25), emission from a 635-nm laser diode (LDH-D-C-640, PicoQuant) was cleaned up (Semrock, FF01-635/18-25), and both lasers were alternated at 30 MHz using a waveform generator (Keysight), a picosecond delayer (Micro Photon Devices) connected to the laser drivers (PDL 800-D). The red laser was delayed by ~20 ns with respect to the blue laser. Linear polarization was cleaned up (Glan-Taylor Polarizer, Thorlabs, GT10-A) and the red and blue light were combined into a single-mode optical fiber (kineFlex, Point Source) before the light (100 μW of 483 nm light and 75 μW of 635 nm light) was reflected into the back port of the microscope (Axiuovert 200, Zeiss) and to the objective (C-APOCHROMAT, 40x/1.2 W, Zeiss). Sample emission was transmitted through a polychroic mirror (Chroma, ZT488/640rpc), focused through a 75-mm pinhole and spectrally split (Semrock FF593-Di03-25x36). The blue range was filtered (Semrock, FF03-525/50-25), and polarization was split (PBS101, Thorlabs) into parallel and perpendicular channels. The red range was also filtered (Semrock, FF01-698/70-25), and polarization was split (PBS101, Thorlabs). Photons were detected on four avalanche photodiodes (SPCM AQR 14, PerkinElmer Optoelectronics, for the green parallel and perpendicular channels and for the red parallel channel and SPCM AQRH 14, Excelitas, for the red perpendicular channel), which were connected to a time-correlated single-photon counting (TCSPC) device (MultiHarp 150N, PicoQuant). Signals were stored in 12-bit first-in-first-out (FIFO) files. Microscope alignment was carried out using fluorescence correlation spectroscopy (FCS) on freely diffusing ATTO 488-CA and ATTO 655-CA (ATTO-TEC). Instrument response functions (IRFs) were recorded one detector at-a-time in a solution of ATTO 488-CA or ATTO 655-CA in near-saturated centrifuged potassium iodide at a 25-kHz average count rate for a total of 25 × 106 photons. Macro Time-dependent microtime shifting was corrected for two (blue/parallel and red/perpendicular) of four avalanche photodiodes (APDs) using the IRF data as input. Data were analyzed using PIE Analysis with Matlab (PAM) software [84] using standard procedures for MFD-PIE smFRET burst analysis [85, 86]. Signals from each TCSPC routing channel (corresponding to the individual detectors) were divided in time gates to discern 483-nm excited FRET photons from 635-nm excited acceptor photons. A two-color MFD all-photon burst search algorithm using a 500-μs sliding time window (minimum of 100 photons per burst, minimum of 5 photons per time window) was used to identify single donor- and/or acceptor–labeled molecules in the fluorescence traces. Double-labeled single molecules were selected from the raw burst data using a kernel density estimator (ALEX-2CDE ≤ 15) that also excluded other artifacts [87]. Sparse slow-diffusing aggregates were removed from the data by excluding bursts exhibiting a burst duration > 12 ms. By generating histograms of E versus measurement time, we corroborated that the distribution of E was invariant over the duration of the measurement. Data was corrected in this order to obtain the absolute stoichiometry parameter S and absolute FRET efficiency E: background subtraction, donor emission crosstalk correction, acceptor direct excitation correction and relative detection efficiency correction. To obtain the relative detection efficiency correction factor (γ), the center values of the E-S data cloud for each protein were estimated manually, plotted in an E vs. 1/S graph, and the data were fit to the following equation where Ω is the intercept and Σ the slope of the linear fit: $\gamma = (\Omega-1)/(\Omega+\Sigma-1)$

Luciferase reporter assays

HEK293T cells (ATCC #CRL-11268) were seeded in a white 96-well plate at 15,000 cells/mL per well. The following day, cells were transfected using Lipofectamine 2000 (Thermo Fisher Scientific) and Opti-MEM with full-length PPARγ2 WT, ΔAF1, W39A, P40A, or empty vector control (pcDNA3.1) expression plasmids (5, 15 or 45 ng for each plasmid with 40, 30 or 0 ng of empty vector respectively to have the same amount of DNA per condition) along with tk-LUC 3X-PPRE luciferase reporter plasmid (45 ng) to a total of 90 ng per well and incubated for 18 hrs at 37 °C, 5% CO_2. The media was aspirated without disturbing the cells then replaced with media supplemented with either 1 μM Rosiglitazone or the same volume of 100% DMSO and incubated 18 hrs at 37 °C, 5% CO_2. The cells were harvested for luciferase activity quantified using Britelite Plus (Perkin Elmer; 25 μL) on a Synergy Neo plate reader (Biotek). Data were plotted as mean ± s.d. in GraphPad Prism; statistics performed using two-way ANOVA with Tukey multiple comparisons analysis and are representative of ≥2 independent experiments.

Western blot analysis

Six wells from each 45 ng HEK293T luciferase reporter assay transfection condition were washed with PBS, pooled, and harvested by centrifugation. Pellets were lysed in TN-T buffer (0.1 M Tris HCl, pH 7.5, 150 mM NaCl, 1% Triton X-100), centrifuged to remove the insoluble fraction, and the total protein in each sample was quantified using a Bradford assay. 40 μg protein/well was run on a 10% SDS-PAGE gel and transferred to PVDF membrane. Membranes were blocked in 5% milk and incubated overnight at 4 ˚C in primary antibody (anti-PPARγ, Santa Cruz #sc-7273; or anti-β-actin, Cell Signaling #3700). Washes were performed in TBS-T (20 mM Tris, 150 mM NaCl, 0.1% Tween-20). Secondary antibody (Jackson ImmunoResearch #115-005-003) was incubated for 1 hr at room temperature. Chemiluminescence was analyzed with SuperSignal West Femto Maximum Sensitivity Substrate (ThermoFisher #PI34095) for PPARγ or luminol reagent (Santa Cruz #sc-2048) for β-Actin using a Bio-Rad ChemiDoc Touch Imaging System. Figures were prepared using Bio-Rad Image Lab Software.

Computational analyses

Disordered structural predictions were performed with ODiNPred [88] using the human PPARγ2 isoform (505 residues). AF-1 secondary structure propensity calculation was performed with SSP [29] using AF-1 Cα and Cβ NMR chemical shift assignments. The net charge per residue of the AF-1 sequence was calculated using localcider (http://pappulab.github.io/localCIDER/) [89]. Predicted PRE profiles from an extended AF-1 conformational ensemble (n=10,000 structures) with no long-range contacts were calculated using flexible-meccano [32].

ACKNOWLEDGMENTS

This work was supported by National Institutes of Health (NIH) grants

R01DK124870 (to D.J.K.) from the National Institute of Diabetes and Digestive and Kidney Diseases (NIDDK/DK); R01AG071332 (to P.R.G.) from the National Institute of Aging (NIA/AG); and R35GM130375 (to A.D.) from the National Institute of General Medical Sciences (NIGMS/GM). The purchase of the 600 MHz NMR instrument was supported in part by NIH grant S10OD021550 from the NIH Office of the Director. S.M. was supported by an NIH/NIDDK predoctoral fellowship (F31DK127643). K.-T.K. was supported by a Farris Foundation Fellowship. D.S. was supported by a postdoctoral fellowship from the Belgian American Educational Foundation. This content is solely the responsibility of the authors and does not necessarily represent the official views of the NIH.

ACCESSION NUMBERS

NMR chemical shift assignments of human PPARγ2 AF-1 (residues 1-135) have been deposited in the Biological Magnetic Resonance Data Bank (BMRB 51507). XL-MS data of full-length PPARγ and ΔAF-1 PPARγ have been deposited in Proteomics Identification Database (PRIDE PXD035304).

AUTHOR CONTRIBUTIONS

S.M. and D.K. conceived and designed the research. S.M., P.M.T., B.M, and X.Y. and expressed and purified proteins and performed NMR. C.C.W. and R.B. performed CD studies. J.B. created mutant plasmids. D.S. and A.A.D. performed smFRET. K.-T.K., T.S.S., and P.R.G. performed XL-MS. D.K. supervised the research and analyzed data along with the other coauthors. S.M. and D.K. wrote the manuscript with input from all authors who approved the final version. The authors declare no conflicts of interest in the completion of this study.

REFERENCES

1. Weikum ER, Liu X, Ortlund EA. The nuclear receptor superfamily: A structural perspective. *Protein Sci.* **27**, 1876–1892 (2018).

2. Kroker AJ, Bruning JB. Review of the Structural and Dynamic Mechanisms of PPARγ Partial Agonism. *PPAR Res.* **2015**, 816856 (2015).

3. Bruning JB, Chalmers MJ, Prasad S, Busby SA, Kamenecka TM, He Y, Nettles KW, Griffin PR. Partial agonists activate PPARgamma using a helix 12 independent mechanism. *Structure*. **15**, 1258–1271 (2007).

4. Shang J, Kojetin DJ. Structural mechanism underlying ligand binding and activation of PPARγ. *Structure*. **29**, 940–950.e4 (2021).

5. Shang J, Brust R, Griffin PR, Kamenecka TM, Kojetin DJ. Quantitative structural assessment of graded receptor agonism. *Proc. Natl. Acad. Sci. U. S. A.* **116**, 22179–22188 (2019).

6. Hughes TS, Chalmers MJ, Novick S, Kuruvilla DS, Chang MR, Kamenecka TM, Rance M, Johnson BA, Burris TP, Griffin PR, Kojetin DJ. Ligand and receptor dynamics contribute to the mechanism of graded PPARγ agonism. *Structure*. **20**, 139–150 (2012).

7. Brust R, Shang J, Fuhrmann J, Mosure SA, Bass J, Cano A, Heidari Z, Chrisman IM, Nemetchek MD, Blayo A-L, Griffin PR, Kamenecka TM, Hughes TS, Kojetin DJ. A structural mechanism for directing corepressor-selective inverse agonism of PPARγ. *Nat. Commun.* **9**, 4687 (2018).

8. Shang J, Mosure SA, Zheng J, Brust R, Bass J, Nichols A, Solt LA, Griffin PR, Kojetin DJ. A molecular switch regulating transcriptional repression and activation of PPARγ. *Nat. Commun.* **11**, 956 (2020).

9. Chandra V, Wu D, Li S, Potluri N, Kim Y, Rastinejad F. The quaternary architecture of RARβ-RXRα heterodimer facilitates domain-domain signal transmission. *Nat. Commun.* **8**, 868 (2017).

10. Chandra V, Huang P, Potluri N, Wu D, Kim Y, Rastinejad F. Multidomain integration in the structure of the HNF-4α nuclear receptor complex. *Nature*. **495**, 394–398 (2013).

11. Chandra V, Huang P, Hamuro Y, Raghuram S, Wang Y, Burris TP, Rastinejad F. Structure of the intact PPAR-gamma-RXR- nuclear receptor complex on DNA. *Nature*. **456**, 350–356 (2008).

12. Lou X, Toresson G, Benod C, Suh JH, Philips KJ, Webb P, Gustafsson J-A. Structure of the retinoid X receptor α-liver X receptor β (RXRα-LXRβ) heterodimer on DNA. *Nat. Struct. Mol. Biol.* **21**, 277–281 (2014).

13. Yu X, Yi P, Hamilton RA, Shen H, Chen M, Foulds CE, Mancini MA, Ludtke SJ, Wang Z, O'Malley BW. Structural Insights of Transcriptionally Active, Full-Length Androgen Receptor Coactivator Complexes. *Mol. Cell*. **79**, 812–823.e4 (2020).

14. Yi P, Wang Z, Feng Q, Chou C-K, Pintilie GD, Shen H, Foulds CE, Fan G, Serysheva I, Ludtke SJ, Schmid MF, Hung M-C, Chiu W, O'Malley BW. Structural and Functional Impacts of ER Coactivator Sequential Recruitment. *Mol. Cell*. **67**, 733–743.e4 (2017).

15. Yi P, Wang Z, Feng Q, Pintilie GD, Foulds CE, Lanz RB, Ludtke SJ, Schmid MF, Chiu W, O'Malley BW. Structure of a biologically active estrogen receptor-coactivator complex on DNA. *Mol. Cell*. **57**, 1047–1058 (2015).

16. Wasmuth EV, Broeck AV, LaClair JR, Hoover EA, Lawrence KE, Paknejad N, Pappas K, Matthies D, Wang B, Feng W, Watson PA, Zinder JC, Karthaus WR, de la Cruz MJ, Hite RK, Manova-Todorova K, Yu Z, Weintraub ST, Klinge S, Sawyers CL. Allosteric interactions prime androgen receptor dimerization and activation. *Mol. Cell* (2022), doi:10.1016/j.molcel.2022.03.035.

17. Jumper J, Evans R, Pritzel A, Green T, Figurnov M, Ronneberger O, Tunyasuvunakool K, Bates R, Žídek A, Potapenko A, Bridgland A, Meyer C, Kohl SAA, Ballard AJ, Cowie A, Romera-Paredes B, Nikolov S, Jain R, Adler J, Back T, Petersen S, Reiman D, Clancy E, Zielinski M, Steinegger M, Pacholska M, Berghammer T, Bodenstein S, Silver D, Vinyals O, Senior AW, Kavukcuoglu K, Kohli P, Hassabis D. Highly accurate protein structure prediction with AlphaFold. *Nature*. **596**, 583–589 (2021).

18. Ruff KM, Pappu RV. AlphaFold and Implications for Intrinsically Disordered Proteins. *J. Mol. Biol.* **433**, 167208 (2021).

19. Tontonoz P, Hu E, Spiegelman BM. Stimulation of adipogenesis in fibroblasts by PPAR gamma 2, a lipid-activated transcription factor. *Cell*. **79**, 1147–1156 (1994).

20. Shao D, Rangwala SM, Bailey ST, Krakow SL, Reginato MJ, Lazar MA. Interdomain communication regulating ligand binding by PPAR-gamma. *Nature*. **396**, 377–380 (1998).

21. Camp HS, Tafuri SR. Regulation of peroxisome proliferator-activated receptor gamma activity by mitogen-activated protein kinase. *J. Biol. Chem.* **272**, 10811–10816 (1997).

22. Hu E, Kim JB, Sarraf P, Spiegelman BM. Inhibition of adipogenesis through MAP kinase-mediated phosphorylation of PPARgamma. *Science*. **274**, 2100–2103 (1996).

23. Adams M, Reginato MJ, Shao D, Lazar MA, Chatterjee VK. Transcriptional activation by peroxisome proliferator-activated receptor gamma is inhibited by phosphorylation at a consensus mitogen-activated protein kinase site. *J. Biol. Chem.* **272**, 5128–5132 (1997).

24. Stechschulte LA, Czernik PJ, Rotter ZC, Tausif FN, Corzo CA, Marciano DP, Asteian A, Zheng J, Bruning JB, Kamenecka TM, Rosen CJ, Griffin PR, Lecka-Czernik B. PPARG Post-translational Modifications Regulate Bone Formation and Bone Resorption. *EBioMedicine*. **10**, 174–184 (2016).

25. Tontonoz P, Hu E, Graves RA, Budavari AI, Spiegelman BM. mPPAR gamma 2: tissue-specific regulator of an adipocyte enhancer. *Genes Dev.* **8**, 1224–1234 (1994).

26. Greenfield NJ. Using circular dichroism spectra to estimate protein secondary structure. *Nat. Protoc.* **1**, 2876–2890 (2006).

27. Greenfield NJ. Using circular dichroism collected as a function of temperature to determine the thermodynamics of protein unfolding and binding interactions. *Nat. Protoc.* **1**, 2527–2535 (2006).

28. Johnson BA, Wilson EM, Li Y, Moller DE, Smith RG, Zhou

G. Ligand-induced stabilization of PPARgamma monitored by NMR spectroscopy: implications for nuclear receptor activation. *J. Mol. Biol.* **298**, 187–194 (2000).

29. Marsh JA, Singh VK, Jia Z, Forman-Kay JD. Sensitivity of secondary structure propensities to sequence differences between alpha- and gamma-synuclein: implications for fibrillation. *Protein Sci.* **15**, 2795–2804 (2006).

30. Mittag T, Forman-Kay JD. Atomic-level characterization of disordered protein ensembles. *Curr. Opin. Struct. Biol.* **17**, 3–14 (2007).

31. Sjodt M, Clubb RT. Nitroxide Labeling of Proteins and the Determination of Paramagnetic Relaxation Derived Distance Restraints for NMR Studies. *Bio Protoc*. **7** (2017), doi:10.21769/BioProtoc.2207.

32. Ozenne V, Bauer F, Salmon L, Huang J-R, Jensen MR, Segard S, Bernadó P, Charavay C, Blackledge M. Flexible-meccano: a tool for the generation of explicit ensemble descriptions of intrinsically disordered proteins and their associated experimental observables. *Bioinformatics*. **28**, 1463–1470 (2012).

33. Scholl D, Sigoillot M, Overtus M, Martinez RC, Martens C, Wang Y, Pardon E, Laeremans T, Garcia-Pino A, Steyaert J, Sheppard DN, Hendrix J, Govaerts C. A topological switch in CFTR modulates channel activity and sensitivity to unfolding. *Nat. Chem. Biol.* **17**, 989–997 (2021).

34. Ferreon ACM, Ferreon JC, Wright PE, Deniz AA. Modulation of allostery by protein intrinsic disorder. *Nature*. **498**, 390–394 (2013).

35. Shen Y, Bax A. Prediction of Xaa-Pro peptide bond conformation from sequence and chemical shifts. *J. Biomol. NMR*. **46**, 199–204 (2010).

36. Schubert M, Labudde D, Oschkinat H, Schmieder P. A software tool for the prediction of Xaa-Pro peptide bond conformations in proteins based on 13C chemical shift statistics. *J. Biomol. NMR*. **24**, 149–154 (2002).

37. Reimer U, Scherer G, Drewello M, Kruber S, Schutkowski M, Fischer G. Side-chain effects on peptidyl-prolyl cis/trans isomerisation. *J. Mol. Biol.* **279**, 449–460 (1998).

38. Li J, Zhang Y, Soubias O, Khago D, Chao F-A, Li Y, Shaw K, Byrd RA. Optimization of sortase A ligation for flexible engineering of complex protein systems. *J. Biol. Chem.* **295**, 2664–2675 (2020).

39. Refaei MA, Combs A, Kojetin DJ, Cavanagh J, Caperelli C, Rance M, Sapitro J, Tsang P. Observing selected domains in multi-domain proteins via sortase-mediated ligation and NMR spectroscopy. *J. Biomol. NMR*. **49**, 3–7 (2011).

40. Chrisman IM, Nemetchek MD, de Vera IMS, Shang J, Heidari Z, Long Y, Reyes-Caballero H, Galindo-Murillo R, Cheatham TE 3rd, Blayo A-L, Shin Y, Fuhrmann J, Griffin PR, Kamenecka TM, Kojetin DJ, Hughes TS. Defining a conformational ensemble that directs activation of PPARγ. *Nat. Commun.* **9**, 1794 (2018).

41. Hughes TS, Wilson HD, de Vera IMS, Kojetin DJ. Deconvolution of Complex 1D NMR Spectra Using Objective Model Selection. *PLoS One*. **10**, e0134474 (2015).

42. Brunmeir R, Xu F. Functional Regulation of PPARs through Post-Translational Modifications. *Int. J. Mol. Sci.* **19** (2018), doi:10.3390/ijms19061738.

43. Li Z, Luo L, Yu W, Li P, Ou D, Liu J, Ma H, Sun Q, Liang A, Huang C, Chi T, Huang X, Zhang Y. PPARγ phase separates with RXRα at PPREs to regulate target gene expression. *Cell Discovery*. **8**, 1–15 (2022).

44. Ikonen T, Palvimo JJ, Jänne OA. Interaction between the amino- and carboxyl-terminal regions of the rat androgen receptor modulates transcriptional activity and is influenced by nuclear receptor coactivators. *J. Biol. Chem.* **272**, 29821–29828 (1997).

45. Langley E, Kemppainen JA, Wilson EM. Intermolecular NH2-/carboxyl-terminal interactions in androgen receptor dimerization revealed by mutations that cause androgen insensitivity. *J. Biol. Chem.* **273**, 92–101 (1998).

46. Berrevoets CA, Doesburg P, Steketee K, Trapman J, Brinkmann AO. Functional interactions of the AF-2 activation domain core region of the human androgen receptor with the amino-terminal domain and with the transcriptional coactivator TIF2 (transcriptional intermediary factor2). *Mol. Endocrinol.* **12**, 1172–1183 (1998).

47. He B, Kemppainen JA, Voegel JJ, Gronemeyer H, Wilson EM. Activation function 2 in the human androgen receptor ligand binding domain mediates interdomain communication with the NH(2)-terminal domain. *J. Biol. Chem.* **274**, 37219–37225 (1999).

48. He B, Kemppainen JA, Wilson EM. FXXLF and WXXLF sequences mediate the NH2-terminal interaction with the ligand binding domain of the androgen receptor. *J. Biol. Chem.* **275**, 22986–22994 (2000).

49. Hur E, Pfaff SJ, Payne ES, Grøn H, Buehrer BM, Fletterick RJ. Recognition and accommodation at the androgen receptor coactivator binding interface. *PLoS Biol.* **2**, E274 (2004).

50. He B, Gampe RT Jr, Kole AJ, Hnat AT, Stanley TB, An G, Stewart EL, Kalman RI, Minges JT, Wilson EM. Structural basis for androgen receptor interdomain and coactivator interactions suggests a transition in nuclear receptor activation function dominance. *Mol. Cell.* **16**, 425–438 (2004).

51. He B, Bowen NT, Minges JT, Wilson EM. Androgen-induced NH2- and COOH-terminal Interaction Inhibits p160 coactivator recruitment by activation function 2. *J. Biol. Chem.* **276**, 42293–42301 (2001).

52. Kraus WL, McInerney EM, Katzenellenbogen BS. Ligand-dependent, transcriptionally productive association of the amino- and carboxyl-terminal regions of a steroid hormone nuclear receptor. *Proc. Natl. Acad. Sci. U. S. A.* **92**, 12314–12318 (1995).

53. Métivier R, Stark A, Flouriot G, Hübner MR, Brand H, Penot G, Manu D, Denger S, Reid G, Kos M, Russell RB, Kah O, Pakdel F, Gannon F. A dynamic structural model for estrogen receptor-alpha activation by ligands, emphasizing the role of interactions between distant A and E domains. *Mol. Cell.* **10**, 1019–1032 (2002).

54. Frank F, Liu X, Ortlund EA. Glucocorticoid receptor condensates link DNA-dependent receptor dimerization and transcriptional transactivation. *Proc. Natl. Acad. Sci. U. S. A.* **118** (2021), doi:10.1073/pnas.2024685118.

55. Rogerson FM, Fuller PJ. Interdomain interactions in the mineralocorticoid receptor. *Mol. Cell. Endocrinol.* **200**, 45–55 (2003).

56. Pippal JB, Yao Y, Rogerson FM, Fuller PJ. Structural and functional characterization of the interdomain interaction in the mineralocorticoid receptor. *Mol. Endocrinol.* **23**, 1360–1370 (2009).

57. Tompa P, Fuxreiter M. Fuzzy complexes: polymorphism and structural disorder in protein-protein interactions. *Trends Biochem. Sci.* **33**, 2–8 (2008).

58. Wright PE, Dyson HJ. Intrinsically disordered proteins in cellular signalling and regulation. *Nat. Rev. Mol. Cell Biol.* **16**, 18–29 (2015).

59. Tzameli I, Fang H, Ollero M, Shi H, Hamm JK, Kievit P, Hollenberg AN, Flier JS. Regulated Production of a Peroxisome Proliferator-activated Receptor-γ Ligand during an Early Phase of Adipocyte Differentiation in 3T3-L1 Adipocytes*. *J. Biol. Chem.* **279**, 36093–36102 (2004).

60. Schmidpeter PAM, Koch JR, Schmid FX. Control of protein function by prolyl isomerization. *Biochim. Biophys. Acta*. **1850**, 1973–1982 (2015).

61. Lummis SCR, Beene DL, Lee LW, Lester HA, Broadhurst RW, Dougherty DA. Cis-trans isomerization at a proline opens the pore of a neurotransmitter-gated ion channel. *Nature*. **438**, 248–252 (2005).

62. Sarkar P, Reichman C, Saleh T, Birge RB, Kalodimos CG. Proline cis-trans isomerization controls autoinhibition of a signaling protein. *Mol. Cell.* **25**, 413–426 (2007).

63. Sarkar P, Saleh T, Tzeng S-R, Birge RB, Kalodimos CG. Structural basis for regulation of the Crk signaling protein by a proline switch. *Nat. Chem. Biol.* **7**, 51–57 (2011).

64. Wang Z, Song J, Milne TA, Wang GG, Li H, Allis CD, Patel DJ. Pro isomerization in MLL1 PHD3-bromo cassette connects H3K4me readout to CyP33 and HDAC-mediated repression. *Cell.* **141**, 1183–1194 (2010).

65. Kubicek K, Cerna H, Holub P, Pasulka J, Hrossova D, Loehr F, Hofr C, Vanacova S, Stefl R. Serine phosphorylation and proline isomerization in RNAP II CTD control recruitment of Nrd1. *Genes Dev.* **26**, 1891–1896 (2012).

66. Zosel F, Mercadante D, Nettels D, Schuler B. A proline switch explains kinetic heterogeneity in a coupled folding and binding reaction. *Nat. Commun.* **9**, 3332 (2018).

67. Gibbs EB, Lu F, Portz B, Fisher MJ, Medellin BP, Laremore TN, Zhang YJ, Gilmour DS, Showalter SA. Phosphorylation induces sequence-specific conformational switches in the RNA polymerase II C-terminal domain. *Nat. Commun.* **8**, 15233 (2017).

68. Favretto F, Flores D, Baker JD, Strohäker T, Andreas LB, Blair LJ, Becker S, Zweckstetter M. Catalysis of proline isomerization and molecular chaperone activity in a tug-of-war. *Nat. Commun.* **11**, 6046 (2020).

69. Gustafson CL, Parsley NC, Asimgil H, Lee H-W, Ahlbach C, Michael AK, Xu H, Williams OL, Davis TL, Liu AC, Partch CL. A Slow Conformational Switch in the BMAL1 Transactivation Domain Modulates Circadian Rhythms. *Mol. Cell*. **66**, 447–457.e7 (2017).

70. Hughes TS, Giri PK, de Vera IMS, Marciano DP, Kuruvilla DS, Shin Y, Blayo A-L, Kamenecka TM, Burris TP, Griffin PR, Kojetin DJ. An alternate binding site for PPARγ ligands. *Nat. Commun.* **5**, 3571 (2014).

71. Bastidas M, Gibbs EB, Sahu D, Showalter SA. A primer for carbon-detected NMR applications to intrinsically disordered proteins in solution. *Concepts Magn. Reson. Part A Bridg. Educ. Res.* **44**, 54–66 (2015).

72. Williamson MP. Using chemical shift perturbation to characterise ligand binding. *Prog. Nucl. Magn. Reson. Spectrosc.* **73**, 1–16 (2013).

73. Ulrich EL, Akutsu H, Doreleijers JF, Harano Y, Ioannidis YE, Lin J, Livny M, Mading S, Maziuk D, Miller Z, Nakatani E, Schulte CF, Tolmie DE, Kent Wenger R, Yao H, Markley JL. BioMagResBank. *Nucleic Acids Res.* **36**, D402–8 (2008).

74. Norris M, Fetler B, Marchant J, Johnson BA. NMRFx Processor: a cross-platform NMR data processing program. *J. Biomol. NMR*. **65**, 205–216 (2016).

75. Johnson BA. From Raw Data to Protein Backbone Chemical Shifts Using NMRFx Processing and NMRViewJ Analysis. *Methods Mol. Biol.* **1688**, 257–310 (2018).

76. Liu F, Lössl P, Scheltema R, Viner R, Heck AJR. Optimized fragmentation schemes and data analysis strategies for proteome-wide cross-link identification. *Nat. Commun.* **8**, 15473 (2017).

77. Kao A, Chiu C-L, Vellucci D, Yang Y, Patel VR, Guan S, Randall A, Baldi P, Rychnovsky SD, Huang L. Development of a novel cross-linking strategy for fast and accurate identification of cross-linked peptides of protein complexes. *Mol. Cell. Proteomics*. **10**, M110.002212 (2011).

78. Liu F, Rijkers DTS, Post H, Heck AJR. Proteome-wide profiling of protein assemblies by cross-linking mass spectrometry. *Nat. Methods*. **12**, 1179–1184 (2015).

79. MacLean B, Tomazela DM, Shulman N, Chambers M, Finney GL, Frewen B, Kern R, Tabb DL, Liebler DC, MacCoss MJ. Skyline: an open source document editor for creating and analyzing targeted proteomics experiments. *Bioinformatics*. **26**, 966–968 (2010).

80. Chen Z, Chen Z, Rappsilber J. A generic solution for quantifying cross-linked peptides using software Skyline. *Protocol Exchange* (2018). , doi:10.1038/protex.2018.001.

81. Chen ZA, Rappsilber J. Quantitative cross-linking/mass spectrometry to elucidate structural changes in proteins and their complexes. *Nat. Protoc.* **14**, 171–201 (2019).

82. Choi M, Chang C-Y, Clough T, Broudy D, Killeen T, MacLean B, Vitek O. MSstats: an R package for statistical analysis of quantitative mass spectrometry-based proteomic experiments. *Bioinformatics*. **30**, 2524–2526 (2014).

83. Combe CW, Fischer L, Rappsilber J. xiNET: cross-link network maps with residue resolution. *Mol. Cell. Proteomics*. **14**, 1137–1147 (2015).

84. Schrimpf W, Barth A, Hendrix J, Lamb DC. PAM: A Framework for Integrated Analysis of Imaging, Single-Molecule, and Ensemble Fluorescence Data. *Biophys. J.* **114**, 1518–1528 (2018).

85. Hellenkamp B, Schmid S, Doroshenko O, Opanasyuk O, Kühnemuth R, Rezaei Adariani S, Ambrose B, Aznauryan M, Barth A, Birkedal V, Bowen ME, Chen H, Cordes T, Eilert T, Fijen C, Gebhardt C, Götz M, Gouridis G, Gratton E, Ha T, Hao P, Hanke CA, Hartmann A, Hendrix J, Hildebrandt LL, Hirschfeld V, Hohlbein J, Hua B, Hübner CG, Kallis E, Kapanidis AN, Kim J-Y, Krainer G, Lamb DC, Lee NK, Lemke EA, Levesque B, Levitus M, McCann JJ, Naredi-Rainer N, Nettels D, Ngo T, Qiu R, Robb NC, Röcker C, Sanabria H, Schlierf M, Schröder T, Schuler B, Seidel H, Streit L, Thurn J, Tinnefeld P, Tyagi S, Vandenberk N, Vera AM, Weninger KR, Wünsch B, Yanez-Orozco IS, Michaelis J, Seidel CAM, Craggs TD, Hugel T. Precision and accuracy of single-molecule FRET measurements—a multi-laboratory benchmark study. *Nat. Methods*. **15**, 669–676 (2018).

86. Kudryavtsev V, Sikor M, Kalinin S, Mokranjac D, Seidel CAM, Lamb DC. Combining MFD and PIE for accurate single-pair Förster resonance energy transfer measurements. *Chemphyschem*. **13**, 1060–1078 (2012).

87. Tomov TE, Tsukanov R, Masoud R, Liber M, Plavner N, Nir E. Disentangling subpopulations in single-molecule FRET and ALEX experiments with photon distribution analysis. *Biophys. J.* **102**, 1163–1173 (2012).

88. Dass R, Mulder FAA, Nielsen JT. ODiNPred: comprehensive prediction of protein order and disorder. *Sci. Rep.* **10**, 14780 (2020).

89. Holehouse AS, Das RK, Ahad JN, Richardson MOG, Pappu RV. CIDER: Resources to Analyze Sequence-Ensemble Relationships of Intrinsically Disordered Proteins. *Biophys. J.* **112**, 16–21 (2017).